Department of Earth and Environmental Sciences
Macquarie University, NSW 2109, Australia
Phone +61 (0)4 77300674
Email maria-constanza.manassero@mq.edu.au

November 15th , 2022

We present an original manuscript entitled " Joint probabilistic inversion of 3D magnetotelluric and seismic data: Lithospheric structure and melting dynamics in southeast Australia" by M.C. Manassero[1], S. Özaydin[1], J. C. Afonso[1,2], J. Shea[1,3], S. Thiel[4,5], A. Kirkby[6], I. Fomin[1] and K. Czarnota[7].

This paper is a non-peer reviewed preprint submitted to EarthArXiv. The preprint is going to be submitted for peer review to Journal of Geophysical Research: Solid Earth on 22th November, 2022.

Yours Sincerely,

Maria Constanza Manassero* (maria-constanza.manassero@mq.edu.au)
Sinan Özaydin (sinan.ozaydin@mq.edu.au)
Juan Carlos Afonso (juan.afonso@mq.edu.au)
Joshua Shea (Joshua.shea1@hdr.mq.edu.au)
Stephan Thiel (Stephan.Thiel@sa.gov.au)
Alison Kirkby (alkirkby@gmail.com)
Ilya Fomin (ilya.fomin@mq.edu.au)
and Karol Czarnota.

[1] Australian Research Council Centre of Excellence for Core to Crust Fluid Systems/GEMOC, Department of Earth and Environmental Sciences, Macquarie University.
[2]Department of Applied Earth Sciences, University of Twente, The Netherlands
[3]Department of Materials, The University of Manchester, Manchester M13 9PL, United Kingdom
[4]Department of Earth Sciences, University of Adelaide, Adelaide, SA 5005, Australia
[5]Geological Survey of South Australia, Adelaide, SA 5001, Australia
[6]GNS Science, Wairakei Research Centre, Taupo, New Zealand
[7]Geoscience Australia, Canberra, ACT, 2601, Australia.

*Corresponding author
Australian Research Council Centre of Excellence for Core to Crust Fluid System (CCFS)
Department of Earth and Environmental Sciences, Macquarie University, Sydney, NSW 2109 , Australia
email: maria-constanza.manassero@mq.edu.au

Joint probabilistic inversion of 3D magnetotelluric and seismic data: Lithospheric structure and melting dynamics in southeast Australia

M.C. Manassero[1], S. Özaydın[1], J.C. Afonso[1,2], J. Shea[1,3], S. Thiel [4,5], A. Kirkby[6], I. Fomin[1]and K. Czarnota[7]

[1]Australian Research Council Centre of Excellence for Core to Crust Fluid Systems/GEMOC, School of Natural Sciences, Macquarie University, Sydney, Australia.
[2]Department of Applied Earth Sciences, University of Twente, The Netherlands
[3]Department of Materials, The University of Manchester, Manchester M13 9PL, United Kingdom
[4]Department of Earth Sciences, University of Adelaide, Adelaide, SA 5005, Australia
[5]Geological Survey of South Australia, Adelaide, SA 5001, Australia
[6]GNS Science, Wairakei Research Centre, Taupo, New Zealand.
[7]Geoscience Australia, Canberra, ACT, 2601, Australia.

Key Points:

- We apply a novel approach for joint probabilistic inversions of 3D magnetotelluric and seismic data.
- We use the new method to image the lithosphere-asthenosphere system beneath southeastern of Australia.
- The imaged lithosphere correlates with the location of volcanic centers and provides insights on the melt production in the region.

Corresponding author: Maria Constanza Manassero, `maria-constanza.manassero@mq.edu.au`

Abstract

The thermochemical structure of the lithosphere exerts control on melting mechanisms in the mantle as well as the location of volcanic eruptions and ore deposits. Imaging the complex interactions between the lithosphere and asthenospheric mantle require the joint inversion of multiple data sets and their uncertainties.In particular, the combination of temperature and electrical conductivity with data proxies for bulk composition and elusive minor phases is a crucial step towards fully understanding large-scale lithospheric structure and melting. We apply a novel probabilistic approach for joint inversions of 3D magnetotelluric and seismic data to image the lithosphere beneath southeast Australia. Results show a highly heterogeneous lithospheric structure that correlates with the location of Cenozoic volcanism and deep conductivity anomalies. In regions where the conductivities have been at odds with sub-lithospheric temperatures and seismic velocities, we observe that the joint inversion provides conductivity values consistent with other observations. The results reveal a strong relationship between metasomatized regions in the mantle and i) the limits of geological provinces in the crust, which elucidates the subduction-accretion process in the region; ii) distribution of leucitite and basaltic magmatism; iii) independent geochemical data, and iv) a series of lithospheric steps which constitute areas prone to generating small-scale instabilities in the asthenosphere. This scenario suggests that shear-driven upwelling and edge-driven convection are the dominant melting mechanisms in eastern Australia rather than mantle plume activity, as conventionally conceived. Our study offers an integrated lithospheric model for southeastern Australia and provides insights into the feedback mechanism driving surface processes.

Plain Language Summary

The lithosphere is the outermost rigid layer of the Earth and the focus of important geological processes such as earthquakes (seismic activity), volcanism, and mineralization. The location of these seismically active zones, magma intrusion/production, and ore deposits often coincide with deep discontinuities in the lithospheric structure. Imaging the structure of the lithosphere using geophysical techniques is then crucial to fully understand the nature of these processes. Obtaining the most reliable images of the lithospheric structure requires the joint analysis of two or more geophysical data sets. In particular, the combination of magnetotellurics (an electromagnetic technique) and seismic data holds great potential due to their complementary sensitivity to the Earth's properties. Combining a joint analysis with a probabilistic approach help us understand the variability of the lithospheric structure better since they provide a large number of models that can explain the data. Given the good data coverage in southeast Australia, we use a new probabilistic approach for the joint analysis of magnetotelluric and seismic data to image the lithosphere structure beneath this region. Our results show a complex lithospheric structure in line with the location of volcanic centers and the tectonic history of the region. Lithospheric composition derived from the models also provides significant insights into how melt production in the area might have occurred.

1 Introduction

Magnetotellurics (MT) has great potential for investigating metasomatism and tectonomagmatic evolution in the lithosphere (e.g., Wannamaker et al., 2008; Comeau et al., 2015; Aivazpourporgou et al., 2015; Wannamaker et al., 2014; Bedrosian, 2016; Blatter et al., 2022; Özaydın & Selway, 2022; Cordell et al., 2022). Imaging the deep thermochemical structure of the lithosphere is crucial due to its connection with surface expressions of fluid and melt pathways, such as the location of ore deposits (e.g., Griffin et al., 2013; Heinson et al., 2018; Kirkby et al., 2022) and volcanic centers (Davies et al., 2015). One of the main limitations of the MT method lies, however, in constraining deep conductivity structures, particularly beneath shallow conductive features. This is due to the the diffusive behaviour of electromagnetic waves and the high sensitivity of MT to conductors (Jones, 1999). The MT method is also ambiguous in discerning the different factors that affect electrical conductivity, such as temperature, water/melt content and composition. Unlocking the full potential of the MT method requires the development of methodologies that can assign meaningful physical interpretations to conductivity anomalies and discriminate between their causes (Selway, 2014).

A widely adopted methodology to reduce feature ambiguity is combining MT with other geophysical data sets via joint inversions (e.g, Khan et al., 2006; Gallardo & Meju, 2007; Jegen et al., 2009; Moorkamp et al., 2010; Afonso, Rawlinson, et al., 2016; Jones et al., 2017). By exploiting the complementary sensitivities of different data sets to the properties of interest, joint inversions minimize the range of acceptable models consistent with the available data and increase model resolution (cf. Moorkamp et al., 2007; Afonso et al., 2013a; Afonso, Rawlinson, et al., 2016; Afonso, Moorkamp, & Fullea, 2016). For example, in the case of MT and seismic data, both data sets are sensitive (to different degrees) to the background thermal and compositional structure of the lithosphere. However, only MT is strongly sensitive to minor conductive phases (e.g., hydrous minerals and graphite), hydrogen content or small-scale melt/fluid pathways (Karato, 1990, 2006; Evans, 2012; Yoshino, 2010; Khan, 2016; Selway, 2014; Manassero et al., 2021). In this way, joint MT+seismic inversions hold great potential for improving the resolution of conductivity structures (e.g., Moorkamp et al., 2007, 2010; Gallardo & Meju, 2007; Afonso, Moorkamp, & Fullea, 2016), detecting the presence of partial melt (cf., Selway & O'Donnell, 2019; Evans et al., 2019) and fluid pathways (cf., García-Yeguas et al., 2017; Bennington et al., 2015) in the lithosphere, and understanding the relationship of these lithospheric features with the location of ore deposits (e.g., Takam Takougang et al., 2015) and metasomatized lithologies (e.g., Snyder et al., 2014).

In addition to the benefits of joint inversions, valuable information about model uncertainties (Tarantola, 2005; Afonso, Rawlinson, et al., 2016; Manassero et al., 2021) can be obtained via probabilistic approaches. These approaches provide a range of models and their probability in explaining the observations by sampling millions of possible models and computing a forward solution for each of them. Thus, probabilistic inversions naturally address the non-uniqueness problem in geophysics (particularly in MT) and quantify model ambiguity (Tarantola, 2005; Gregory, 2005; Rosas-Carbajal et al., 2013). Given their intrinsic computational cost, simulation-based probabilistic approaches are limited to problems where fast forward operators are available. In the case of 3D MT inversions, fully probabilistic methods have been infeasible due to the large CPU time required by the associated forward problem (Miensopust et al., 2013). In order to address this limitation, Manassero et al. (2020) developed a novel strategy, referred to as RB+MCMC, that allows obtaining fast and accurate approximations of the forward solution and performing joint probabilistic inversions of 3D MT data with other data sets (Manassero et al., 2021). Potential applications and the efficiency of the method to solve the joint inverse problem of MT and seismic data were previously demonstrated with whole-lithosphere synthetic examples in our previous paper (Manassero et al., 2021).

In this work, we apply the new method to the dense MT and seismic data sets in south-eastern Australia to provide new constraints on its complex lithospheric structure. This region has undergone several episodes of accretion-subduction and extension processes (Glen, 2005), lithospheric deformation (Moresi et al., 2014) and contains part of the mafic Eastern Australian Volcanic Province (EAVP), one of the most voluminous intraplate volcanic regions in the world (Johnson et al., 1989; Sutherland et al., 2012). The EAVP is somewhat unique since half its volcanism is age-progressive and commonly linked to a hot mantle plume (e.g., Sutherland et al., 2012; Davies et al., 2015), whereas the remaining half is not age-progressive with no obvious melting mechanism (Wellman & McDougall, 1974). To further exacerbate this issue, lava compositions throughout the

EAVP (including both age-progressive and non-age-progressive volcanic centers) argue for low-temperature melting of metasomatized mantle source lithologies. In contradiction to the presence of a hot mantle plume, these compositions suggest a source driven by mild perturbations in mantle temperatures (Shea et al., 2022), such as shear-driven upwelling and edge-driven convection (Davies & Rawlinson, 2014; Demidjuk et al., 2007). Since thermo-physical variations in the lithosphere exert control on melt composition and eruption locations (Davies et al., 2015), reliable models of the lithospheric first-order structure are necessary to explain these controversies.

Independent results from conventional ambient noise and teleseismic tomography (Rawlinson et al., 2016; Davies et al., 2015; Young et al., 2013), xenolith thermobarometry (e.g., Lu et al., 2018), thermal modeling (e.g., Tesauro et al., 2020) and a recent 3D conductivity model (Kirkby et al., 2020) have yielded important information about the lithospheric structure beneath southeast Australia. However, some discrepancies are observed between these models despite the fact that they all describe the same region. Beneath the Eastern Volcanics, for example, the sub-lithospheric mantle conductivities in the model of Kirkby et al. (2020) are at odds with the mantle temperatures inferred by Tesauro et al. (2020) and the low velocities imaged by Rawlinson et al. (2016) and Davies et al. (2015). In this work, we attempt to bridge the results of independent studies and obtain reliable lithospheric models that are compatible with independent geophysical, geological, and geochemical evidence in south-eastern Australia. In particular, we aim to assess how the lithospheric structure may have influenced melting mechanisms for the EAVP and to better understand overall melting dynamics in intraplate settings.

To achieve these goals, we use our probabilistic approach to obtain thermal, seismic velocity, and electrical conductivity models (with their uncertainties) by jointly inverting 3D magnetotelluric data and seismic velocities from a tomographic model (Rawlinson et al., 2016). Bulk water content maps are derived from the inversion results to further understand the connection between geodynamic processes and metasomatism.

2 Geological background

The Tasmanides in eastern Australia are a complex orogenic system that developed from west to east through repetitive cycles of subduction and accretion along the eastern margin of Gondwana (Glen, 2005, 2013; Champion et al., 2016; Rosenbaum, 2018). This region is broadly divided into the Delamerian Orogen in the west (early-Palaeozoic) and the younger (mid-Paleozoic) Lachlan Orogen in the southeast (Figure 1.a). Much of the geological complexity in the area can be explained by a geodynamic model of a micro-continent collision and later development of an orocline, referred to as the Lachlan Orocline model (Cayley, 2011; Cayley & Musgrave, 2015; Moresi et al., 2014; Musgrave, 2015). The major structures described in this model are curved crustal geometries with an eastward rotation that persists below the base of the crust (Musgrave, 2015), which have been imaged by gravity, magnetic, and potential field data (e.g., Musgrave & Rawlinson, 2010; Nakamura & Milligan, 2015; Nakamura, 2016, see Figure 1.c-d,); ambient noise tomography in the crust (e.g., Young et al., 2013; Pilia et al., 2015, see Figure 10.d); 2D MT conductivity models (Aivazpourporgou et al., 2015) and a recent 3D MT conductivity model (Kirkby et al., 2020; Heinson et al., 2021). This latter 3D conductivity model shows, for the first time, that some of those crustal structures persist below the Moho, providing new insights about the lithospheric architecture and geodynamic history of the region.

Throughout the late Mesozoic and the entire Cenozoic, eastern Australia has been consistently subjected to voluminous mafic intraplate volcanism, which formed the extensive Eastern Australian Volcanic Province (EAVP, Johnson et al., 1989; Sutherland et al., 2012; Shea et al., 2022). Several regions throughout northern and south-eastern Australia contain recent eruptions; in northern Australia, the Kinrara vent contains lavas

$\sim$7 ka $\pm$ 2 ka (Cohen et al., 2017), while the Mount Gambier, Newer Volcanics (NV) contains lavas $\sim$ 4–7.5 ka (Blackburn et al., 1982; Smith & Prescott, 1987).

The EAVP comprises 67 separate volcanic centers with two dominant volcanic center compositions: basalt and potassic leucitite (Figure 1.b). While basaltic volcanics erupted through thinner lithosphere ($<$ 110 km) along the eastern and south-eastern seaboard, the leucitite volcanic centers lie on thick lithosphere ($>$ 125 km) in central New South Wales and central Victoria (Davies & Rawlinson, 2014; Rawlinson et al., 2017). This leucitite suite represents the most petrologically atypical and extraordinarily enriched melt compositions reported for mafic melts in eastern Australia (Cundari, 1973; Birch, 1978). Particularly, they represent melts from the most pervasively metasomatized source assemblages, likely a Ti-bearing oxide phlogopite websterite $\pm$ apatite (Shea et al., 2022), which deviate from anhydrous peridotites. A review of the intra-continental volcanic centers in the EAVP and their source assemblages is presented in Shea et al. (2022). The lack of anhydrous peridotite and the abundance of hydrous minerals in their mantle source assemblages is of particular importance to this work, indicating widespread mantle metasomatism beneath eastern Australia.

3 Methods and data sets

3.1 Data

The data used in our joint probabilistic inversion include magnetotelluric (MT) data from the AusLAMP array (Australian Lithospheric Architecture Magnetotelluric Project) in southeast Australia and the P-wave velocity model of Rawlinson et al. (2016) as seismic data. The long-period MT data were acquired at 298 AusLAMP stations (blue triangles in Figure 1.f) across a $\sim$55 km spaced array covering an area of 950 $\times$ 950 km. Details about the data acquisition and processing are given in Kirkby et al. (2020). The MT data are the full impedance tensor for periods between 6.4 to 40,000s. Error floors are set to 5% of $\max(|Z_{xx}|, |Z_{xy}|)$ for the components Z_{xx} and Z_{xy} and 5% of $\max(|Z_{yy}|, |Z_{yx}|)$ for the components Z_{yy} and Z_{yx}. We assume uncorrelated data errors that follow a double exponential distribution (e.g., Farquharson & Oldenburg (1998); Rosas-Carbajal et al. (2013); Manassero et al. (2021)).

The P-wave velocity model used in this study (Rawlinson et al., 2016) was constructed from teleseismic tomography using data from the mainland component of the WOMBAT transportable seismic array (Rawlinson et al., 2015). In order to account for the unresolved crustal component of the teleseismic arrival time residuals, the model includes a detailed crustal model from ambient noise tomography (Young et al., 2013) and the Moho from AuSREM (Kennett & Salmon, 2012) in the starting model. Using this model, we obtain seismic velocities on a data-point grid of 50$\times$50 km at the surface (shown in red dots in Figure 1.f) and 24 points between the surface and 340 km depth. The data errors are assumed to be uncorrelated and normally distributed with a standard deviation of 1% of the velocity. Examples of data and data fits for MT data and seismic velocities are shown in Figures 2 and 3, respectively. Additional figures can be found in the Supplementary Material.

3.2 Bayesian inversion and model parameterization

In the Bayesian or probabilistic approach to the inverse problem, inference about the model parameters $\mathbf{m}$, given observed data $\mathbf{d}$, is based on the so-called posterior probability density function (PDF):

$$P(\mathbf{m}|\mathbf{d}) = \frac{P(\mathbf{d}|\mathbf{m})P(\mathbf{m})}{P(\mathbf{d})} \propto \mathcal{L}(\mathbf{m})P(\mathbf{m}) \propto exp(\phi)P(\mathbf{m}), \tag{1}$$

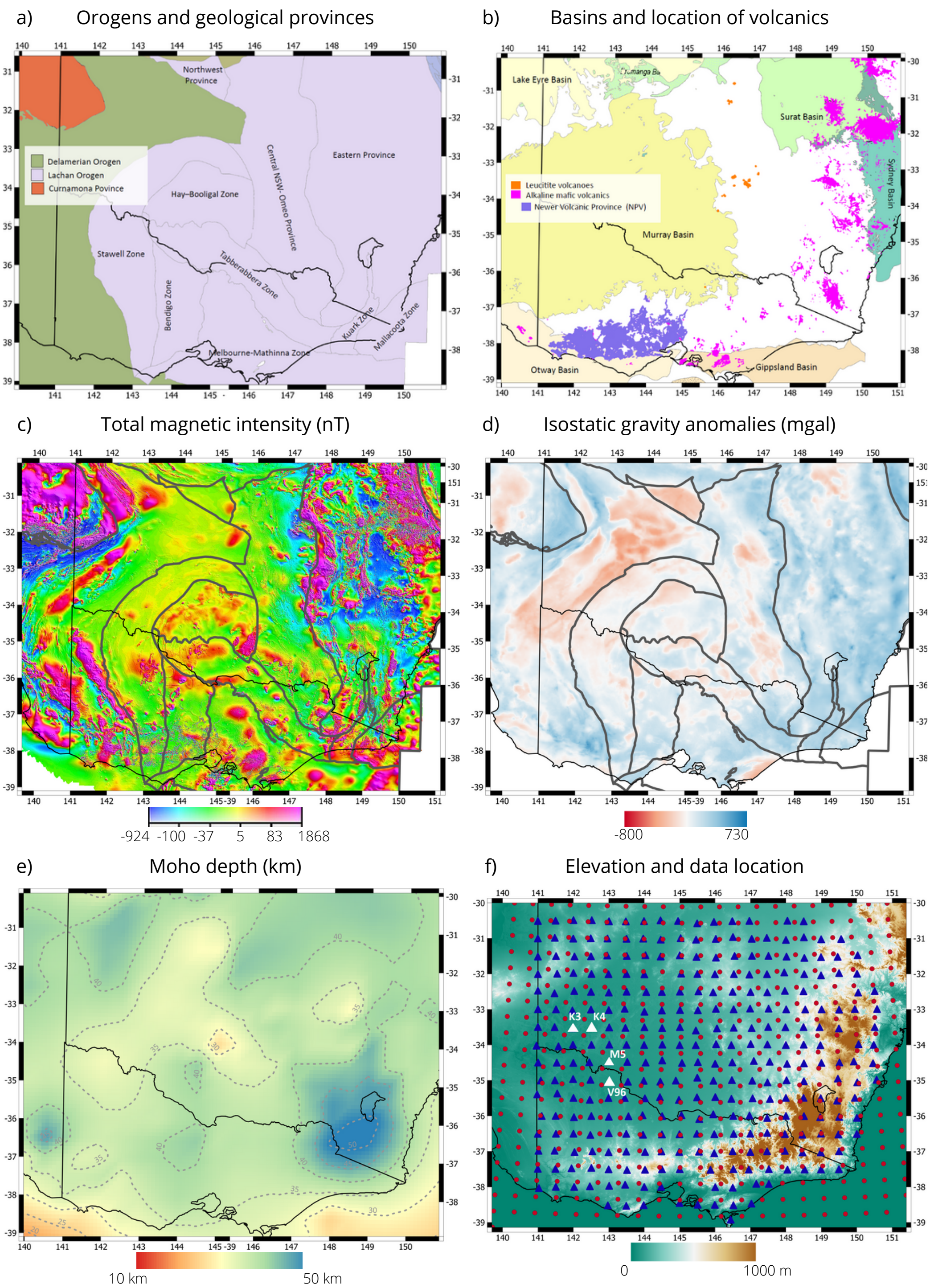

Figure 1. Maps showing (a) orogens that comprise the Tasmanides of southeastern Australia with grey outline denoting geological provinces (Raymond et al., 2018); (b) Mesozoic to Cenozoic sedimentary basins after Raymond et al. (2012), leucitites volcanoes (orange) and basaltic volcanics (pink) after Shea et al. (2022). The basaltic in NV are highlighted in purple. (c) Total magnetic intensity map (TMI) which includes airborne-derived TMI data for onshore and near-offshore continental areas (Nakamura & Milligan, 2015). (d) Isostatic residual anomaly map (Nakamura, 2016). (e) Moho depth from the AusREM model (Kennett & Salmon, 2012) where 5km-contour lines are shown in dashed-grey. (f) Elevation map of southeast Australia including the AusLAMP MT stations (blue triangles) and the location of the velocity data (red dots). Panel (c) and (d) show major tectonic boundaries are outlined in grey. White triangles indicate stations where data fits are shown.

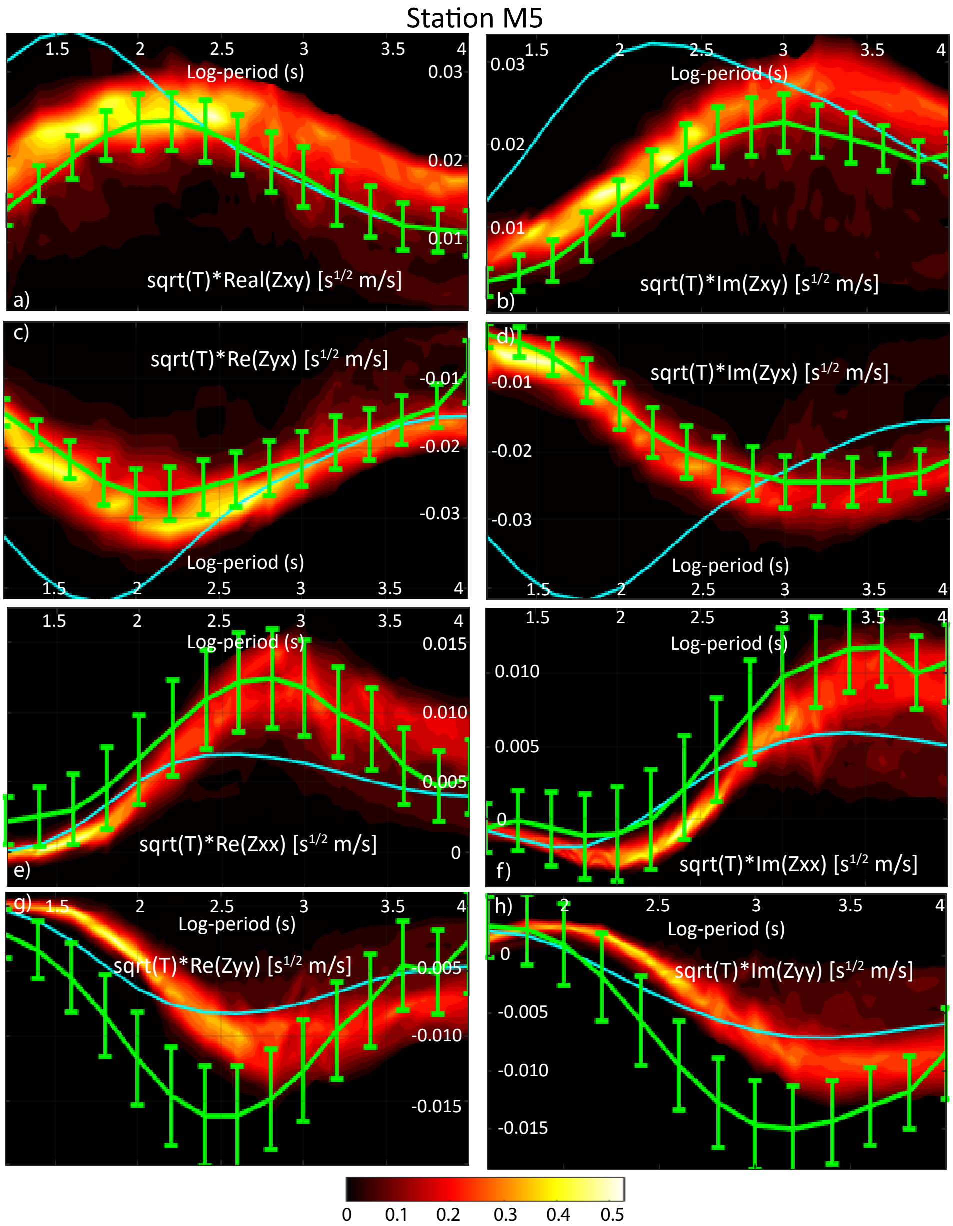

Figure 2. Posterior PDFs (refer to next section) of MT data for station M5. Field data and error bars are plotted in green and the computed data for the initial model is plotted in blue. Panels (a), (b), (c) and (d): Posterior PDFs of the real and imaginary parts of the off-diagonal components (Zxy and Zyx). Panels (e), (f), (g) and (h): Posterior PDFs of the real and imaginary parts of the diagonal components (Zxx and Zyy). The data has been scaled by the square-root of the period (T) in all panels. The location of the station is shown in Figure 1.f

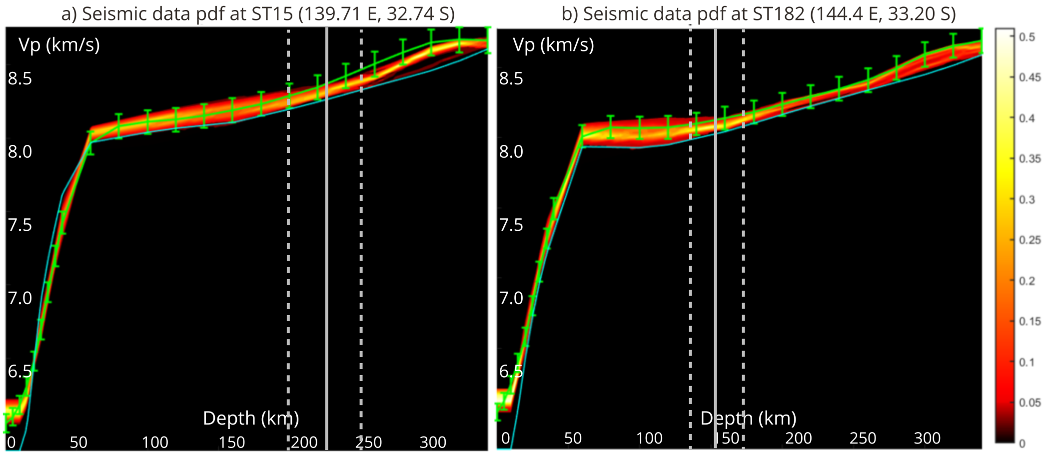

Figure 3. Posterior PDFs (refer to next section) of P-wave velocity data for stations (a) ST15 located at 139.71 E, 32.74 S and (b) ST182 at 144.4 E, 33.20 S. P-wave velocity data and error bars are plotted in green and the computed data for the initial model is plotted in blue. For those locations, the LAB depths corresponding to the mean, lower and upper bound of the 68% CI models are shown in solid and dashed grey lines, respectively.

where $P(\mathbf{m})$ denotes the prior PDF describing all the information on the model's parameters prior to the inversion (e.g., prior geological or petrological knowledge in the area of study). $\mathcal{L}(\mathbf{m})$ is the likelihood function, which is specified by the statistical distribution of the data errors, and ϕ is the *misfit* of model $\mathbf{m}$. In the case of MT, the data misfit is given by (Tarantola, 2005):

$$\phi = -\sum_{i=1}^{N} \frac{|g_i(\mathbf{m}) - d_i(\mathbf{m})|}{s_i}, \tag{2}$$

whereas the misfit for the seismic data takes the following form:

$$\phi = -\frac{1}{2}\sum_{i=1}^{N} \Big(\frac{g_i(\mathbf{m}) - d_i(\mathbf{m})}{s_i}\Big)^2. \tag{3}$$

For each data set, $\mathbf{g}$ is the solution of a particular forward problem for model $\mathbf{m}$, N is the total number of data and s_i denotes the standard deviation for the *i-th* data error.

The posterior PDF over data and parameters is commonly approximated using sampling-based Markov chain Monte Carlo (MCMC) algorithms (Gilks et al., 1995). In our joint inversions of independent data sets, we use the Delayed Rejection Adaptive Metropolis (DRAM) scheme of Haario et al. (2006) in combination with the Cascaded Metropolis (CM) approach (Tarantola, 2005; Hassani & Renaudin, 2013; Manassero et al., 2021). Details about the general inversion framework (RB+MCMC) are given in Manassero et al. (2021) while particular details about the sampling strategy, prior information and initial model used for the current inversion are given in Appendix A.

In order to define the model parameters of the inversion, we treat the conductivity and seismic velocities in the mantle as a superposition of two contributions: *background* properties related to the long-wavelength thermo-physical state of the dry mantle and *anomalous* conductivity features associated with the presence of water content, hydrous minerals, grain-boundary graphite films, interconnected sulfides, melts or metasomatized regions (Manassero et al., 2021). A particular realization of the background is defined using a column-based parameterization which includes the depth to the thermal lithosphere-astenosphere boundary (LAB) and thermal nodes placed in the sub-lithospheric mantle of individual columns. This parameterization is used for both the seismic and MT forward solution. We also use a second parameterization, within the MT problem only, based on electrical conductivity nodes to account for the conductivity in the crust and those conductivity anomalies over the background (see details in Appendix C and in Manassero et al., 2021).

We incorporate one conductivity cell below each MT station as an extra parameter of the inversion to account for the galvanic distortion effect produced by near-surface inhomogeneities that are below the resolution of our model (Jones, 2011; Chave & Jones, 2012; Avdeeva et al., 2015). Similarly to the methodology used in ModEM (Kelbert et al., 2014), these cells are placed in the first (thin) layer of the numerical mesh used to solve the MT forward problem.

The crustal structure used within the seismic models consists of three crustal layers per column (upper crust/sediments, middle crust, and lower crust). Each layer has a fixed thickness and its own set of physical properties: coefficient of thermal expansion, isothermal compressibility, thermal conductivity, bulk density, volumetric radiogenic heat production (RHP), thickness, P-wave (V_p) and S-wave (V_s) velocities, and V_p/V_s ratio. Whilst all of these can be included as parameters of the inversion, in this work, the unknowns are the V_p of each crustal layer. The layers' densities are computed from V_p assuming Brocher's empirical law (Brocher, 2005) while V_s is obtained from the sampled V_p and the prior information on V_p/V_s ratios.

Information about the model parameters (i.e., LAB depths, temperature nodes, V_p velocity in the crust and conductivity nodes) and their uncertainties can be obtained by exploring the posterior PDF. For example, we can estimate the mean model and the models corresponding with the lower and upper bounds of the 68 % confidence interval (CI) of the posterior PDF. This interval corresponds with the range of models that fall within one standard deviation from the mean, and is commonly used as an indicator of model uncertainty. This complete information is later used to obtain models in terms of the thermophysical properties of the whole lithosphere, such as seismic velocities, electrical conductivity and water content.

3.3 Forward Problems and Model Discretization

Most of the forward problems solved during the probabilistic inversion (MT forward in 3D, heat transfer and surface wave dispersion curves) have been described in detail in Manassero et al. (2020, 2021) and in Afonso et al. (2013a, 2013b); Afonso, Rawlinson, et al. (2016). Subsequently, we focus on the model discretization and derivation of the seismic velocity and background conductivity models from the model parameters.

The study area is subdivided into 441 columns of size $0.45° \times 0.45° \times 410$ km, where each column is discretized at three different scales:

1. The finest discretization scale makes up the fine mesh (2 km) to solve the seismic forward operators (surface waves and seismic models) and the steady-state conductive geotherm in the lithosphere.
2. The intermediate discretization comprises the finite elements (FE) used to solve the MT forward problem. In this case, we use $63 \times 63 \times 36$ FE elements of size 17×17 km in the horizontal and variable vertical size with depth. The air comprises four FE cells and a total thickness of 106 km.
3. The thermal nodes constitute the coarser discretization used to obtain mantle-stable mineral assemblages and the corresponding physical properties (e.g., seismic velocities, bulk density). In this study, the thermal nodes are placed every 50 km in the vertical direction.

The thermo-physical properties at the thermal nodes are obtained by interpolating the properties from pre-computed tables at the nodes' specific composition, sampled temperature and pressure (computed using a quadratic lithostatic-type approximation, see Appendix B). In order to compute these tables, we use components of the software PerpleX (Connolly, 2009; Afonso et al., 2013b) to solve the Gibbs free-energy minimization problem together with the database and thermodynamic formalism of Stixrude & Lithgow-Bertelloni (2011) within the CFMAS system ($CaO - FeO - MgO - Al_2O_3 - SiO_2$). All thermophysical properties computed at the thermodynamic nodes are linearly interpolated to the fine mesh for the computation of the seismic forward operator and to the FE mesh for the computation of the MT forward solution (see details in Appendix B).

3.4 Mantle composition

The equilibrium assemblages are computed using a mean bulk mantle composition (i.e., specific CFMAS compositions) of 44.3 wt% SiO_2, 2.8 wt% Al_2O_3, 8.5 wt% $Fe_2\mathrm{O}_3$, 39.3 wt% MgO and 2.7 wt% CaO. We estimate this mean composition by averaging eight spinel lherzolites xenoliths (see Table S1 in Supplementary material) that were entrained in EAVP lavas. We use major element compositions from Irving (1980), O'Reilly & Griffin (1987), Griffin et al. (1987) and unreported samples from Bokhara River (J. Shea, personal communications), which cover the area of interest. Since this is the most recent volcanism in eastern Australia, these xenoliths are the most representative samples of current mantle compositions available.

The vast majority of xenoliths in eastern Australia equilibrated at pressures < 2 GPa (O'Reilly & Griffin, 1985; Pearson et al., 1991; Sutherland et al., 1994). However, the CFMAS compositions used here are close to the continental mantle (McDonough, 1990): fertile peridotites (Boyd, 1989b) and pyrolite (Ringwood, 1962). Suggesting these xenoliths have not been modally metasomatized, and their CFMAS concentrations are equilibrated with upper mantle peridotites, which allows for their average to be used as an estimate for current mantle compositions beneath eastern Australia. We note that in cratonic regions, the average mantle compositions may resemble harzburgitic or dunitic compositions (Boyd, 1989b).

The use of an average mantle composition is justified by the fact that the seismic velocities and electrical conductivity have second-order sensitivity to dry bulk mantle composition (see Figure S1, S2 and Özaydın & Selway, 2020; Trampert et al., 2001; Goes et al., 2000). We also assume a dry mantle composition for the background properties. The reason for this is that, firstly, the seismic velocities are not affected by small amounts of water commonly observed in mantle samples (Yu et al., 2011, and references therein) as the actual phase compositions are insensitive to water contents bound to minerals (Cline Ii et al., 2018). Secondly, since the conductivity nodes represent any conductivity value that departs from the background (dry resistive mantle), this choice allows us to sample only positive anomalies and reduce the number of parameters by two (see Manassero et al., 2021).

3.5 Mantle water content

Using outputs of the joint probabilistic inversion (thermal structure and conductivity models) and the mean mantle composition described above, we obtain estimations of the bulk water content in the mantle (i.e. hydroxyl or OH^- bound to nominally anhydrous minerals) as a proxy for mantle metasomatism. These estimations are made using the software MATE (Özaydın & Selway, 2020), which includes several experimental models for electrical conductivity, water partitioning and solubility (based on petrological studies). In particular, we used the electrical conductivity models of Gardés et al. (2014a), Dai & Karato (2009a), Liu et al. (2019), and Dai & Karato (2009c) for olivine, orthopyroxene, clinopyroxene and garnet, respectively.

The solutions for the water content lie between the bounds defined by the dry lithosphere (i.e., 0 ppm) and the maximum bulk water content calculated using the olivine water solubility model of Padrón-Navarta & Hermann (2017). The experimental coefficients used in the water partitioning are: $D^{OH}_{opx/ol} = 5.6$, $D^{OH}_{cpx/opx} = 1.9$ of Demouchy et al. (2017) and $D^{OH}_{gt/ol} = 0.8$ of Novella et al. (2014); which reflect the sub-solidus conditions found in the continental lithospheric mantle in southeastern Australia. Since we aim to portray variations of water content in the mantle rather than fitting the real water content seen in xenoliths, the choice of the experimental parameters is adequate for our calculations. All water calculations are made using the calibration of Withers et al. (2012) for olivine, and the calibration of Bell et al. (1995) for pyroxenes and garnet.

The electrical conductivity of each individual phase is turned into bulk conductivity through the Generalised Archie's Law (Glover, 2010) with cementation components (m) of $m = 2$ for orthopyroxenes, $m = 4$ for clinopyroxenes and garnet, and $m < 1$ for olivine (perfectly connected). The Generalised Archie's Law is preferred over the conservative estimates of Hashin-Shtrikman lower-bound since it allows us to incorporate the effects of specific minerals in the conductivity values, such as highly-interconnected phlogopites. The main cementation components used here, however, provide similar values to the Hashin-Shtrikman lower-bound for a lherzolitic matrix (Özaydın & Selway, 2020).

4 Results

4.1 Thermal structure of Southeast Australia

The depth to the thermal LAB (1250^oC, Afonso, Rawlinson, et al., 2016) obtained from the joint probabilistic inversion of seismic velocities and MT data is shown in Figure 4, while the complete 3D temperature structure is shown via depth slices in Figure 5 (first three columns). Figure 4 also includes a recent LAB model obtained from a 1D joint probabilistic inversion of elevation, surface heat flow, Rayleigh wave dispersion curves, and geoid anomalies using LitMod1D (Haynes et al., 2020; Afonso et al., 2013b); and the estimated LAB depths from two recent seismic tomography models in eastern Australia (Davies et al., 2015; Rawlinson et al., 2017). These results reveal a highly heterogeneous lithospheric structure beneath the Tasmanides: while shallow LAB depths (< 100 km) are imaged on the eastern and south edges of the model, deeper LAB depths (> 250 km) are found beneath the Curnamona Province (CP) and the northern part of the Delamerian Orogen. We observe that the lithospheric structure is also in agreement with the locations of recent volcanism (e.g., Figure 4.a): the leucitite volcanic centers correlate with regions of an intermediate lithospheric thickness (125-160km) while the basaltic volcanoes are located in regions where the LAB depth is less than 120 km. The most distinctive features are step-like changes in the LAB depth from the CP to the southeast corner of the model.

The LAB model is in good agreement with the mean LAB obtained using LitMod1D (Afonso et al., 2013a, 2013b; Haynes et al., 2020), even though the data sets used in each inversion are completely different. The first-order LAB structure is also in agreement with the LAB depths derived from seismic velocity models (Davies et al., 2015; Rawlinson et al., 2017). In particular, we observe similar LAB depths beneath the basaltic volcanoes and west of 146^oE, where a wedge-like structure follows the curvature of the Stawell Zone (SZ, see Figure 3.1). There is a clear discrepancy in the center of the models where our inversion yields shallower mean LAB depths (< 150 km). The LAB of Davies et al. (2015) falls, however, within the model uncertainties of our inversion. Even though we use the model of Rawlinson et al. (2016) as data, the reason for this discrepancy is that our inversion directly samples temperature and favors dynamic features (instead of a thick conductive LAB) in order to fit all constraining data sets simultaneously.

The main difference between our LAB depths and the models of (Davies et al., 2015; Rawlinson et al., 2017) is that we observe deeper LAB depths beneath CP. At first, this difference could be attributed to the fact that the composition in this cratonic area is more depleted than the average bulk mantle composition used here (see Section 3.3) and deeper LAB depths are needed to fit the fast seismic velocities in this region. However, the seismic velocities computed for a cratonic composition (abyssal peridotite after Boyd, 1989a) are comparable to those computed with the average bulk composition used in the lithosphere (Figure S3a, Supplementary Material). Given the good data fit for the seismic velocities in the region (Figure S3b), we note that the LAB depths found beneath CP are consistent with the Paleoproterozoic-Archean origins of this cratonic region (Page et al., 2005; Hand et al., 2008).

The depths to the thermal LABs obtained after an RB+MCMC probabilistic inversion using MT data only are shown in Figures 6. Compared to the results from the joint inversion, these figures show large variability and lack of structure in the LAB models. This comparison elucidates the fact that MT alone provides low sensitivity to discriminate the temperature from other factors controlling the conductivity. Given the poor constraints provided by MT, it becomes evident that other types of data sets (e.g., seismic) are necessary to image the thermal lithospheric structure properly.

4.2 Seismic velocity structure

Depth slices of the P-wave velocity structure predicted by our model are shown in Figure 5. The P-wave velocity model of Rawlinson et al. (2016) is also included as a reference. In all cases, the velocities are plotted relative to the AusREM model at $34.4^oS, 145^oE$ (Figure S4 in Supplementary Material). We observe that the inversion succeeded in reproducing the V_p structure found in the model of Rawlinson et al. (2016). In particular, the mean P-wave velocity down to 100 km is practically identical in both models. Interestingly, the Newer Volcanic province stands out as a low-velocity anomaly at depths between 60 and 80 km. On the other hand, the basaltic volcanoes in the middle of the Eastern Province ($\sim 149^oE$, 34^oS) correlate well with deep low-velocity anomalies.

Some minor discrepancies are observed at depths below 100 km between our results and the model of Rawlinson et al. (2016). For instance, we obtain slightly higher seismic velocities (0.6% higher on average) at depths from 100 to 180 km at the eastern end of the model. Whilst most of these differences fall within the model uncertainties, they can be mostly attributed to the constraints imposed by the MT in the joint inversion. Similarly, we obtain slightly slower velocities throughout the whole model at 200-220 km depth (see Figure 5). At these depths, the local discrepancies are simply explained by the use of different physical parameterizations.

4.3 Electrical conductivity structure

The conductivity models for the crust and mantle predicted by the joint inversion are shown in Figures 7, 8 and 9. For comparison, these figures include the results obtained from a recent deterministic inversion of MT data (Kirkby et al., 2020), using the ModEM software (Kelbert et al., 2014). The main structures observed in the conductivity models are comparable (within model uncertainties) to those in the model of Kirkby et al. (2020) at all depths.

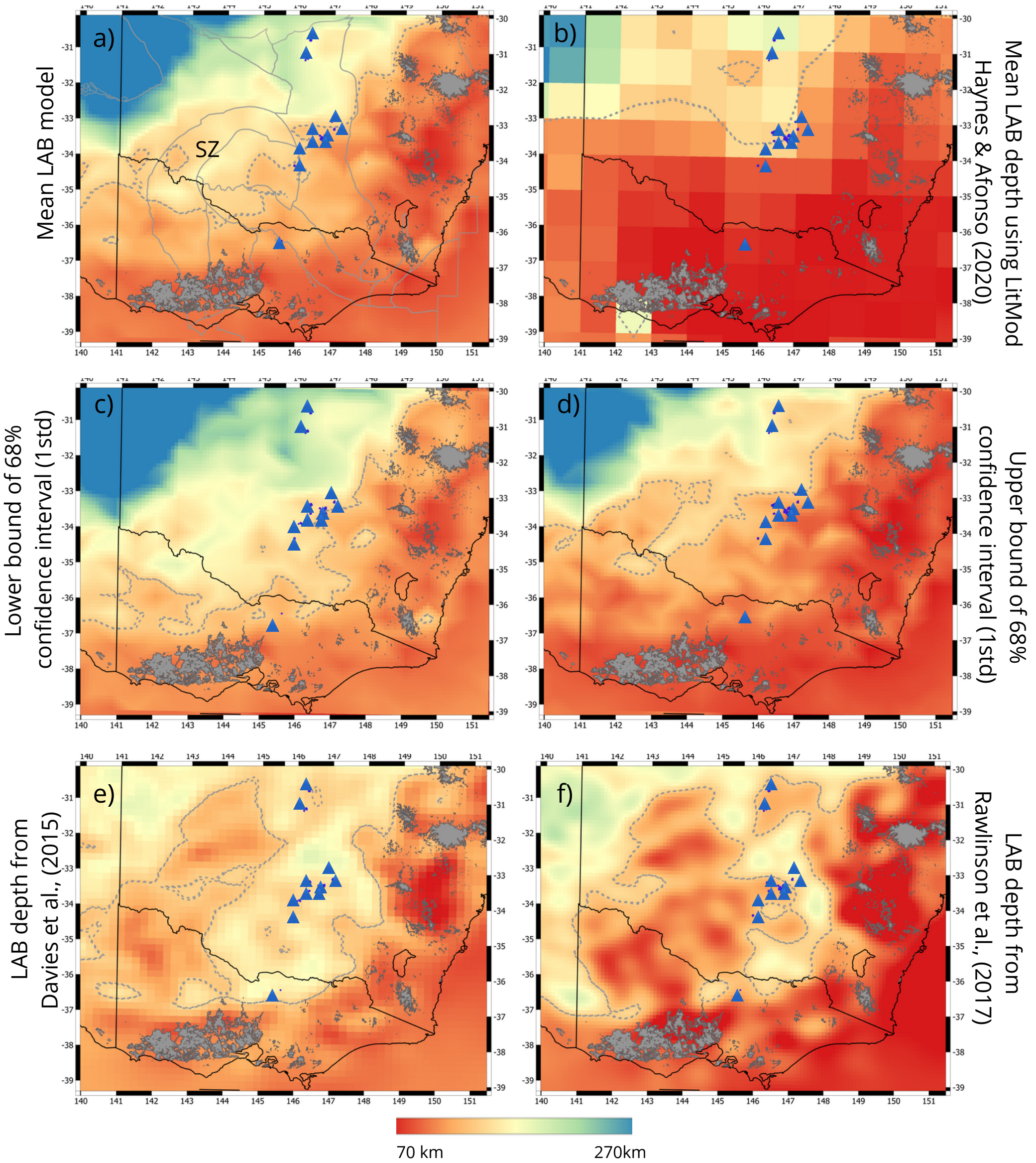

Figure 4. Depth of the thermal LAB. (a) Mean model after the joint probabilistic inversion; (b) mean model obtained after a 1D joint probabilistic inversion (Haynes et al., 2020; Afonso et al., 2013b); (c) and (d) lower and upper bounds of the 68 % confidence interval (1 standard deviation from the mean), respectively. (e) and (f) depth of the LAB after Rawlinson et al. (2017) and Davies et al. (2015), respectively. The location of leucitite-bearing volcanism are shown in blue and standard basaltic volcanoes in grey. The 140 km-contour of the LAB depth in shown in dashed-grey line and the outline of the tectonic provinces in solid grey lines. The location of the Stawell Zone (SZ) is marked in panel (a).

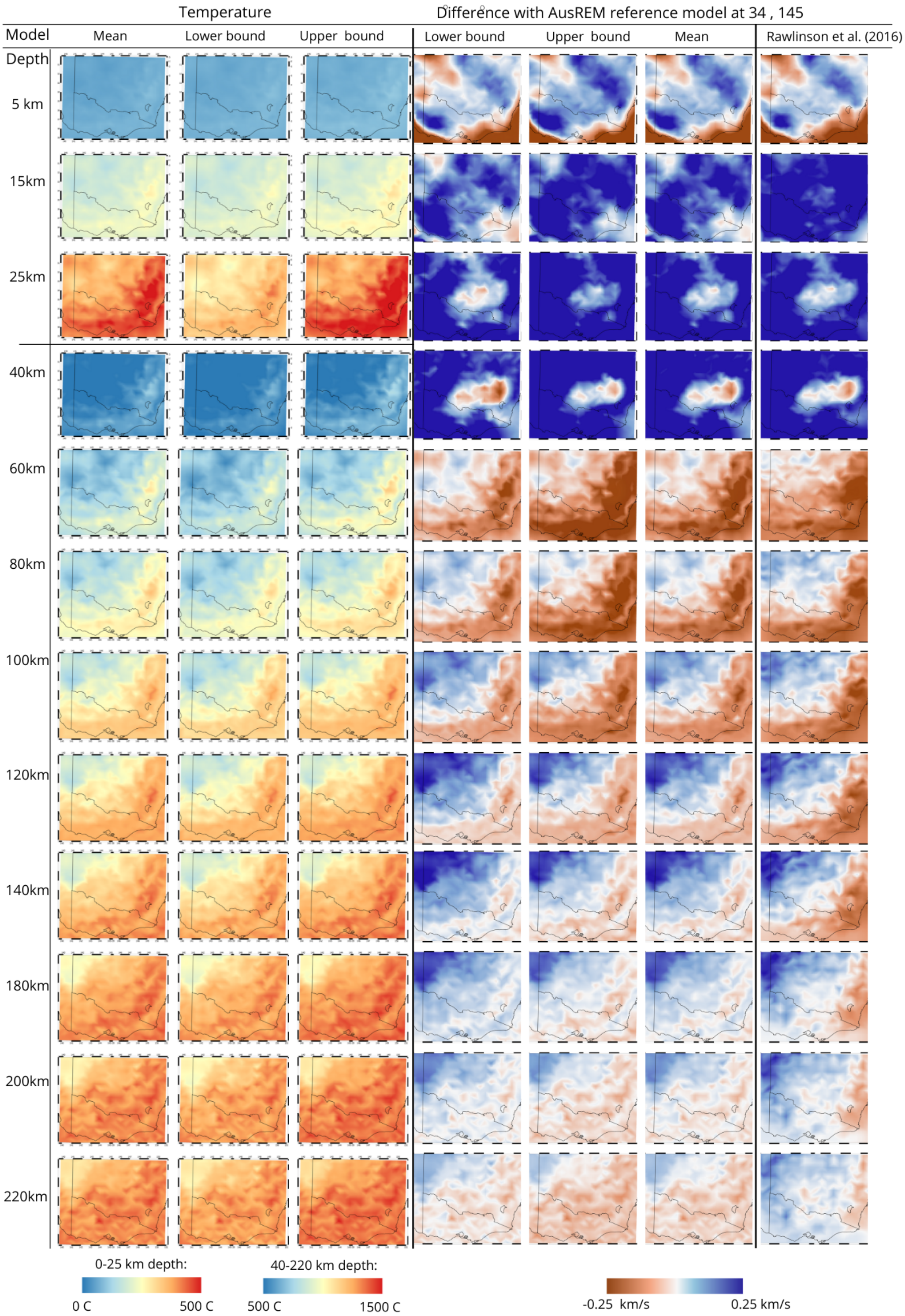

Figure 5. Columns (1)-(3): depth slices from the (1) mean model and those models corresponding to (2) the lower and (3) upper bound of the 68% CI of the posterior PDF for the temperature. Columns (4)-(6): depth slices from the models corresponding to (4) the lower and (5) upper bound of the 68% CI, and (6) mean of the posterior PDF for the P-wave velocity; Column (7): P-wave velocity model of (Rawlinson et al., 2016). Selected depths are shown on the left of the figure. In all cases, velocities are plotted relative to 1-D reference model AusREM at $34.4^o S, 145^o E$ shown in Figure S4 of the Supplementary Material.

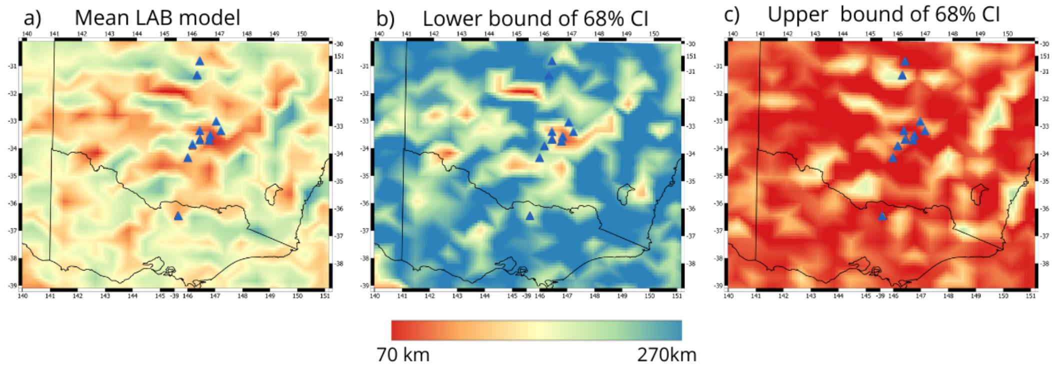

Figure 6. LAB depth from a probabilistic inversion of MT data only. (a) Mean, (b) lower and (c) upper bounds of the 68 % confidence interval. The location of leucitite volcanoes are shown in blue triangles.

4.3.1 Crust

Figures 10 indicate the agreement between the conductivity structure in the crust and independent information: sedimentary basins (Raymond et al., 2012), magnetic anomalies (Nakamura & Milligan, 2015) and a shear velocity model (Pilia et al., 2015). In particular, Panel (a) shows that the extent of the Paleozoic to Cenozoic sedimentary basins in the region is well outlined by the mean conductivity model at 2 km depth. A visual comparison between Panels (c,e,f) and Panel (b) shows the correlation between total magnetic anomalies and conductivity features at different depths. Examples of these are (A) a conductor in the CP; (B) a SW-NE linear structure close to the NW limit of Murray Basin; conductors (C) and (D) in the Tabberabbera Zone; (E) a N-S conductor aligned with the western border of the Eastern Province; (F) two resistive structures west of the Sydney Basin; (G) the Sydney Basin; (H) a conductive region aligned with the north limit of the Northwest and Central NSW provinces; (I) a highly resistive region in the Stawell Zone near the NSW-VIC border; (J) a circular structure in the middle of the model; (K) a high-conductivity anomaly; and (L) a conductor east of CP.

The conductor (A) correlates well with the conductor seen in the MT study of Robertson et al. (2016), using data from 74 AusLAMP stations placed in the Ikara–Flinders Ranges and CP, and in the recent study of Kay et al. (2022), using a densely-spaced MT modeling scheme. Comparing Panels (c) and (d), we observe that the structures (A)-(G) correlate well with low and high-velocity regions imaged by the shear-wave velocity model of Pilia et al. (2015). We note that the concentric geometries at 29 km depth, such as conductor (J) and structures on the west of the model, resemble the features of the Lachlan Orocline model revealed by potential field and passive seismic data (c.f. Kirkby et al., 2020).

4.3.2 Mantle

The similarities between the mantle conductivity models at ∼40-80 km depth and features found in the gravity anomalies (Nakamura, 2016) are shown in Figures 11. These features are: the conductor (A); a conductor (M) in the northwest of the Tabberabbera Zone; two conductivity lineaments (N and O); and a linear conductor (P) placed at the border between the Stawell Zone and the Delamerian Orogen.

The conductivity models between 80-250 km depth (Figures 8 and 9) largely resemble the ModEM model of Kirkby et al. (2020). In particular, we observe a similar north-eastward orientation of the conductors in the middle of the model (C_1,C_2,C_3, C_4 and C_5 in Figure 9). Comparing the mantle conductivity with the mean LAB structure in (Figures 12), our models suggest that there is a good alignment between the LAB topography and these mantle conductors (cf. Kirkby et al., 2020). Notably, C_5 aligns well with the LAB wedge northwest of the model, C_{3N} and C_4S follow the 140 km LAB depth iso-surface while C_1,C_2 and C_3S align with LAB depths < 120 km. We also observe a deep high-conductivity structure beneath the CP (C_6), which agrees well with the structure imaged by previous MT studies (e.g., Robertson et al., 2016; Thiel & Heinson, 2013). A high-conductivity region (C_4) is observed below the central-leucitite volcanoes. In our models, the extent of this region is larger and more connected than in the ModEM model.

The main difference we observe between our conductivity model and the model Kirkby et al. (2020) is that the sub-lithospheric conductivities along the south-east coast and in the middle of the model are higher than those values found in the model of Kirkby et al. (2020) (R_1 and R_2 in Figures 9) and in the models from a probabilistic inversion of MT data only (Figure S5, Supplementary Material). The high resistivity ($> 10^4\Omega m$) in these regions have been at odds with the mantle resistivity range obtained for sub-lithospheric temperatures and pressures (Fullea et al., 2011; Naif et al., 2021). We observe that, due to the favorable constraint of the seismic data to the thermal structure in the joint probabilistic inversion, these high resistivity values are not permissive anymore.

Another example of the favorable constraint imposed by the seismic data in the conductivity models is shown in Figures 12. At 140 km depth, we observe that the conductors in the east (C_1, C_2 and C_{3S} in Figure 12.c) are located within a region defined by a 1250^{o}C-contour (Figure 12.b). These mantle conductivity structures correlate well with both the location of the eastern basaltic volcanics and a stripe of low P-wave seismic velocities (Figure 12.d). At the same time, the stripe of high seismic velocities beneath the east coast at a depth of 140 km is a clear example of the constraint imposed by the MT data in the velocity models. This stripe is not seen in the models of Rawlinson et al. (2016) and correlates with a relatively cold and highly resistive mantle (Figures 12.b-c).

4.4 Joint assessment of bulk water content and temperature maps

One of the key benefits of our inversion is that we can dissociate the effects of the temperature and other factors controlling the conductivity structures, such as water content. The bulk water content maps derived from the mantle conductivity models are shown in Figures 13 and 14. We observe that most of the localized conductive anomalies above the background are likely to contain high percentages of bulk water content. This is the case for the following structures depicted in Figure 14: C_1, C_2 and C_3 beneath the eastern basaltic volcanoes; C_4 below the central leucitites; C_5 on the eastern boundary of Delamerian Orogen; C_6 beneath CP; and the deep localized conductor C_7 at $\sim -30.5^oN, 147^oE$.

Figures 15-17 and Figure S6 show vertical slices of the conductivity, water content and temperature along four transects depicted in Panel (b) of Figure 12. The transects in Figure 15 cross most of the geological provinces on the west and demonstrate a striking correlation between the geological boundaries and the alternation between wet/dry portions of the lithosphere. The joint assessment of these transects clearly shows that the lithospheric mantle beneath CP (C_6) corresponds with a highly conductive, hydrated, and cold region. We observe a high-conductivity anomaly (C_5) below the Stawell Zone that crosses the LAB. While the high temperatures found in this region (T_2 in Figure 15c) can partially explain the conductivity of this structure, Figure 15b indicates that a large part of its conductivity is related to the presence of water content. Similarly, the high-conductivities observed in the region C_{3N} (beneath Tabberrabberra Zone) and the conductor C_{NV1} (at ~90 km depth beneath the NV) are entirely explained by a large amount of water content.

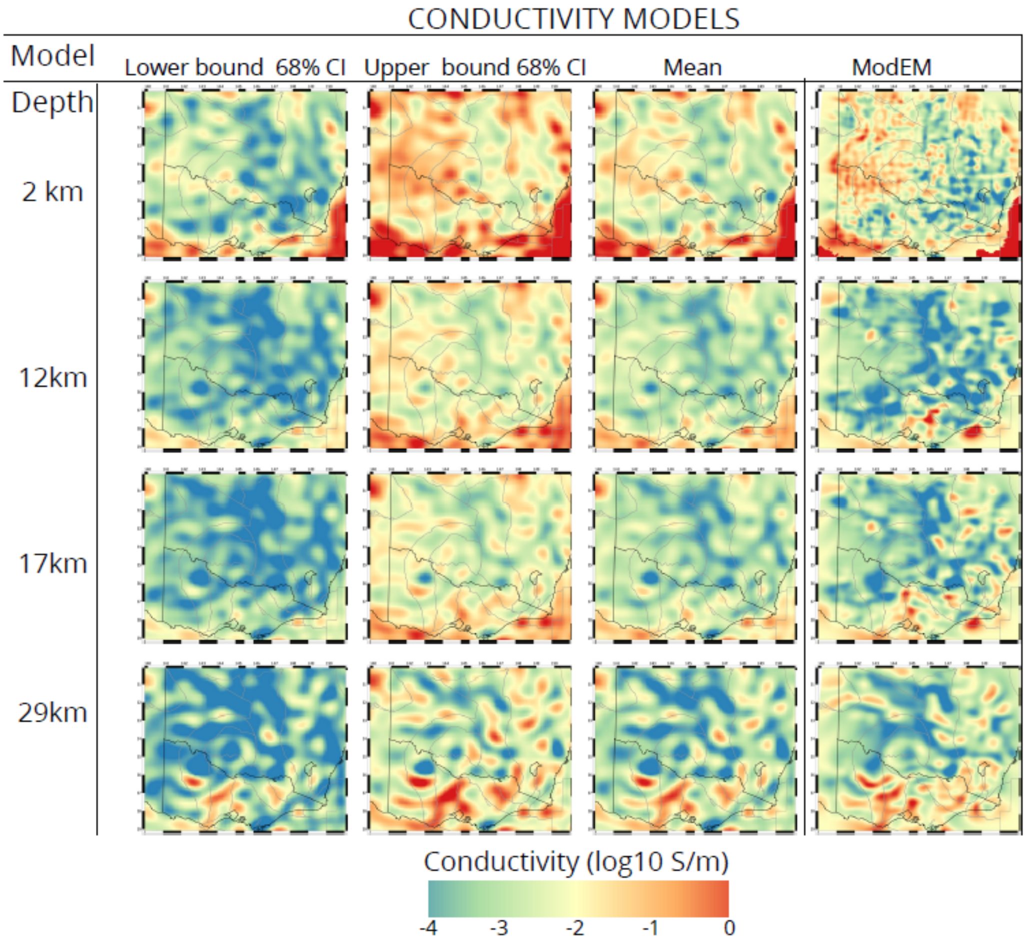

Figure 7. Conductivity in the crust from the joint probabilistic inversion. Columns (1)-(3): depth slices from the (1) the lower, (2) upper bound of the 68% percentile and (3) mean conductivity models of the posterior PDF. Column (4): conductivity model of (Kirkby et al., 2020). Selected depths are shown on the left of the figure and the boundaries of geological provinces are shown in grey lines.

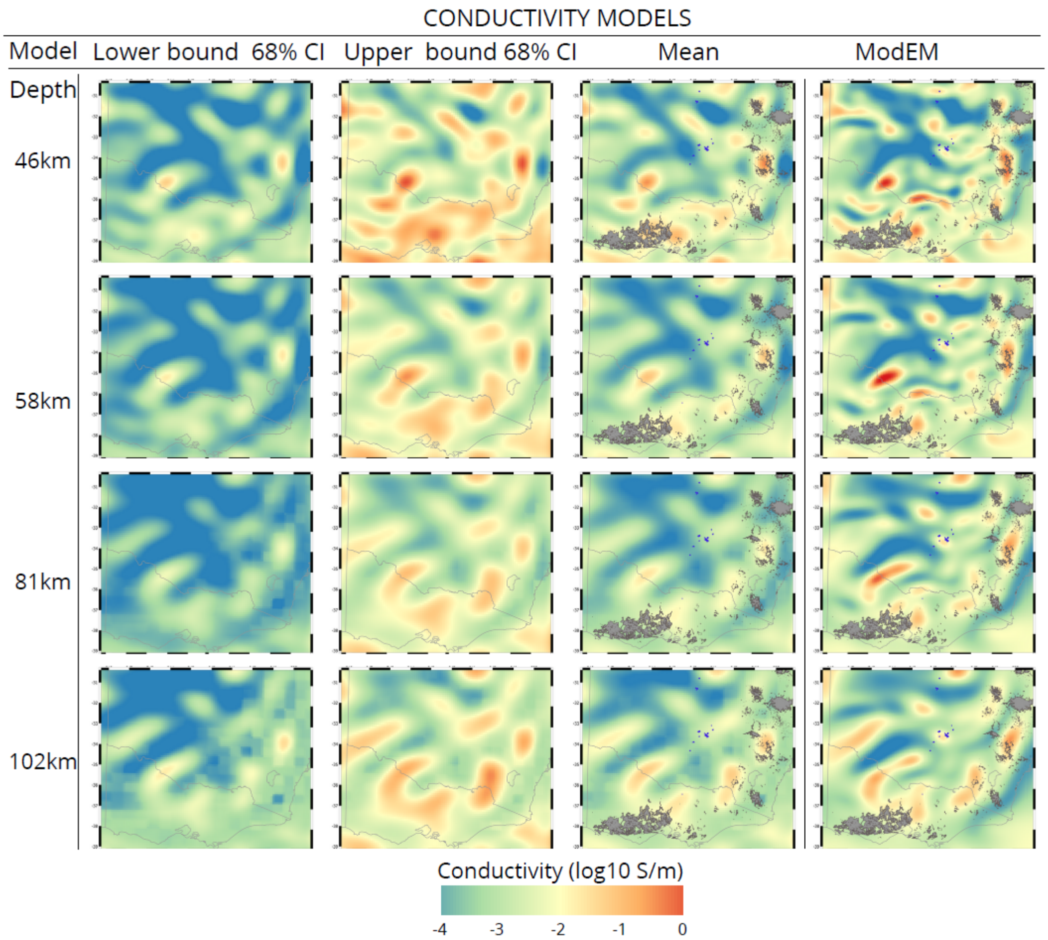

Figure 8. Mantle conductivity from the joint probabilistic inversion. Columns (1)-(3): depth slices from the (1) the lower, (2) upper bound of the 68% percentile and (3) mean conductivity models of the posterior PDF. Column (4): conductivity model of Kirkby et al. (2020). The location of leucitite- bearing volcanism are shown in blue and standard basaltic volcanoes in grey. Selected depths are shown on the left of the figure.

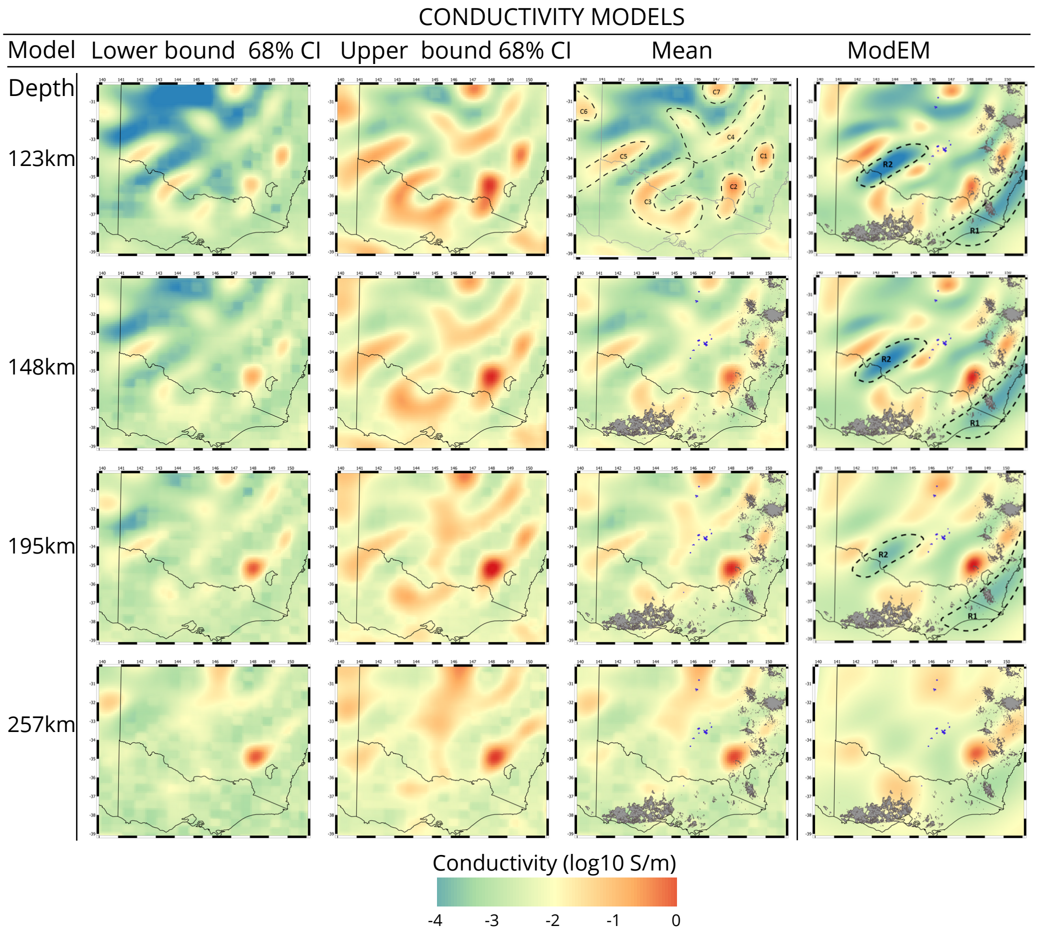

Figure 9. Mantle conductivity from the joint probabilistic inversion. Columns (1)-(3): depth slices from the (1) the lower, (2) upper bound of the 68% percentile and (3) mean conductivity models of the posterior PDF. Column (4): conductivity model of Kirkby et al. (2020). The location of leucitite- bearing volcanism are shown in blue and standard basaltic volcanoes in grey.Selected depths are shown on the left of the figure. Dashed-black lines highlight conductors in the mean model and resistors in the ModEM model at 123 km depth.

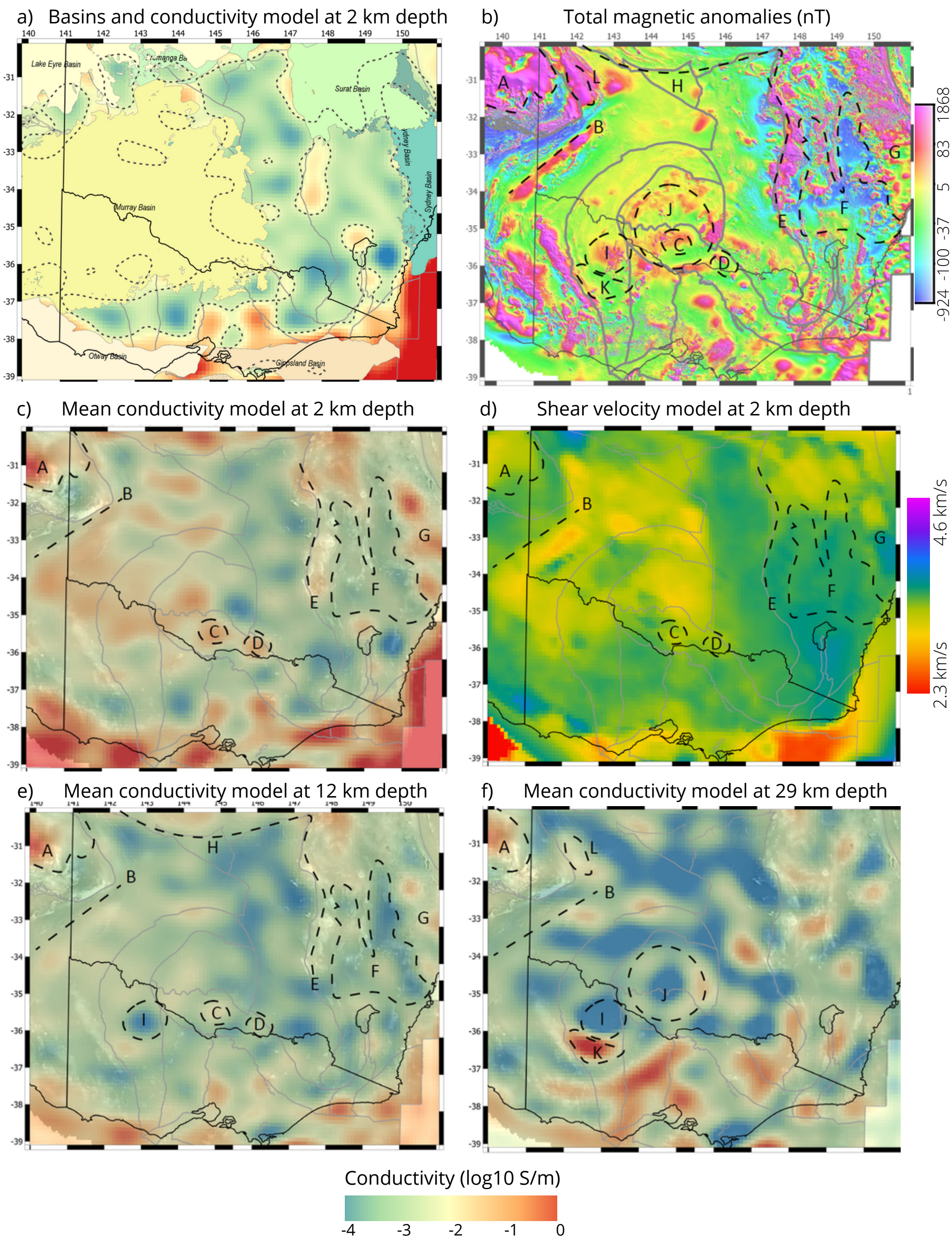

Figure 10. (a) Sedimentary basins overlying mean conductivity model at 2 km depth and 200 Ωm-resistivity contour in dash lines. (b) Total magnetic anomalies after Nakamura & Milligan (2015) (c) Mean conductivity and (d) share wave velocity model after Pilia et al. (2015) at 2 km depth. (e-f) Mean conductivity models at 12 and 29 km depth. We refer the reader to the main text for a description of structures A-L. Boundaries of geological provinces are shown in grey lines.

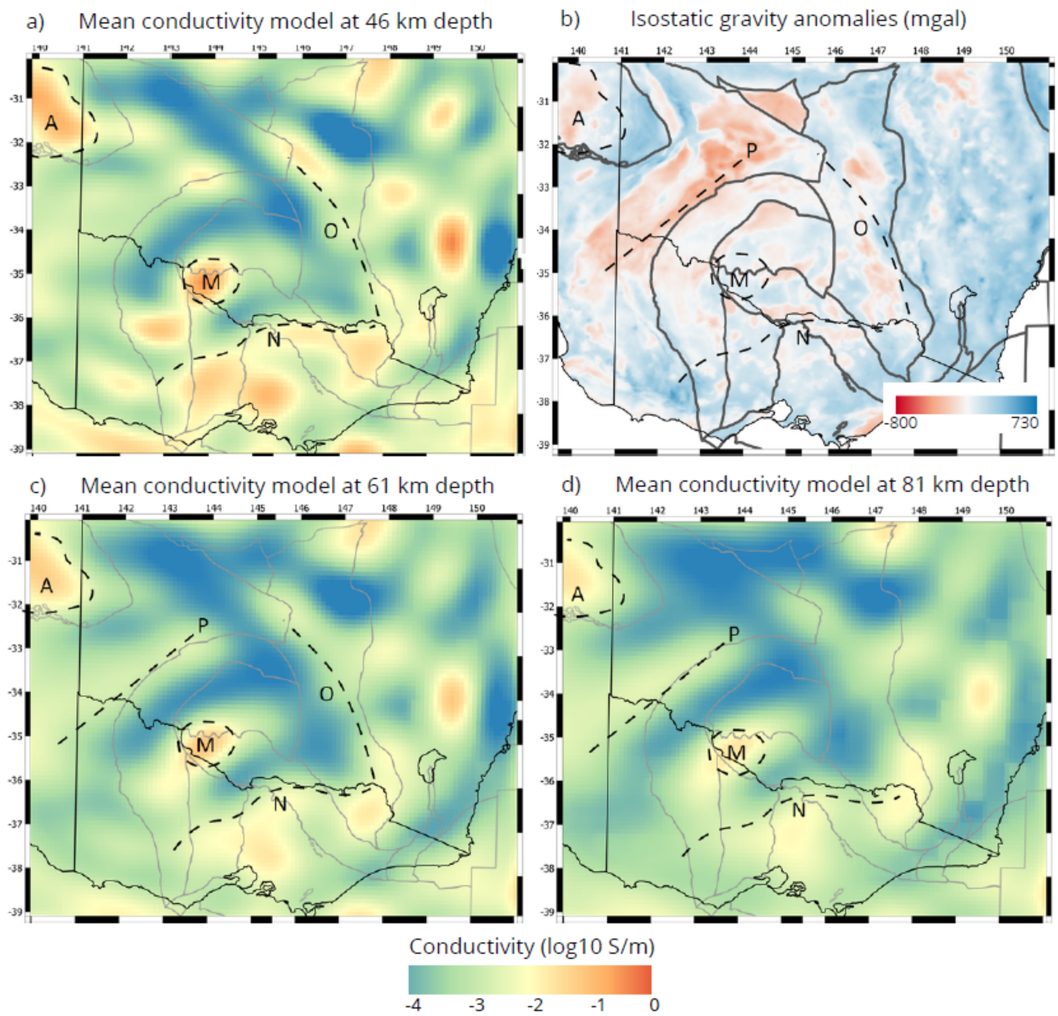

Figure 11. (a), (c) and (d) Mean conductivity models at 46, 61 and 81 km depth, respectively. (b) Isostatic gravity anomalies after Nakamura (2016). We refer the reader to the main text for a description of structures M-P. Boundaries of geological provinces are shown in grey lines.

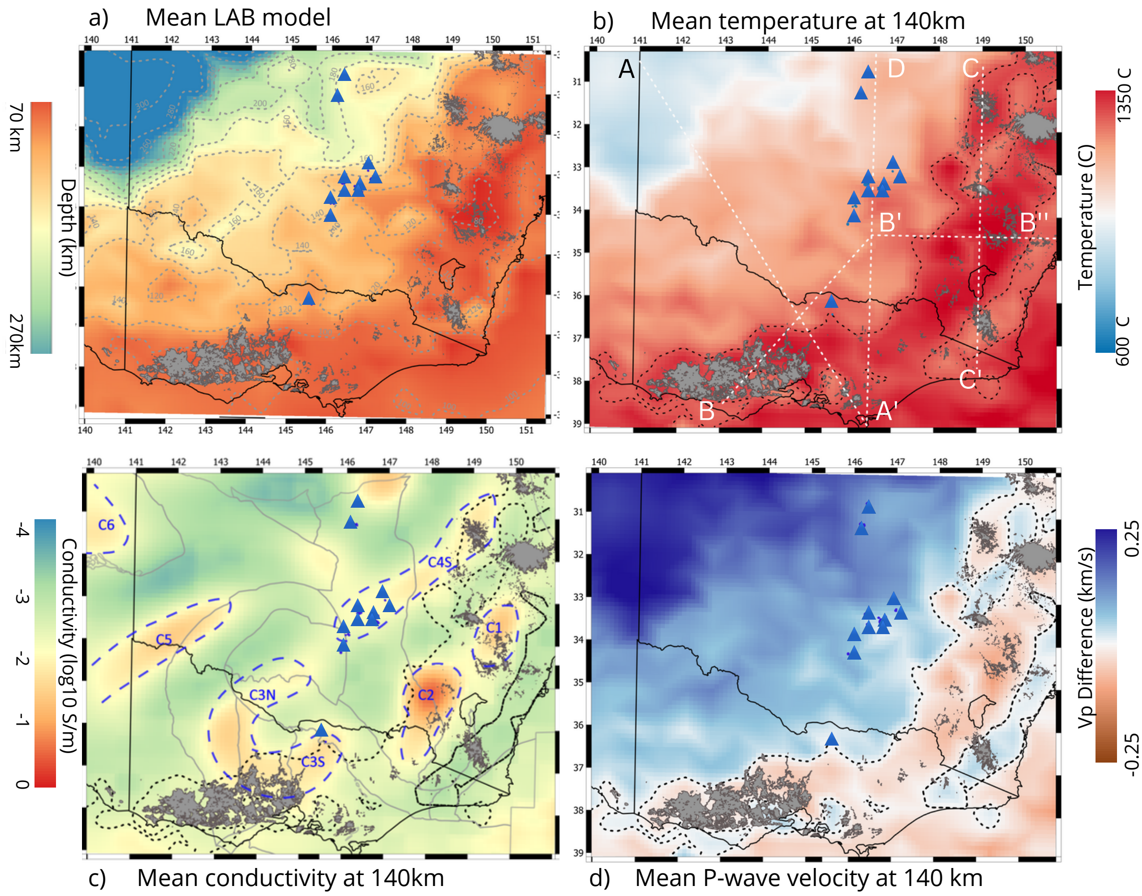

Figure 12. (a) Mean LAB depth. Contours of the LAB depth every 20 km are shown in grey-dashed line. Mean models at 140 km of (b) temperature (c) electrical conductivity and (d) P-wave velocity relative to 1-D reference model AusREM at $34.4^oS, 145^oE$. The 1250^oC-contour (corresponding with the thermal LAB) is plotted in dashed-black in (b-d). Panel (c) shows the location of the geological provinces and conductors in dashed blue. The location of leucitite volcanoes are shown in blue triangles and the surface outcrop of basaltic volcanics are shown in grey in all panels. Panel (b) shows five transects which are discussed in section 5.1.

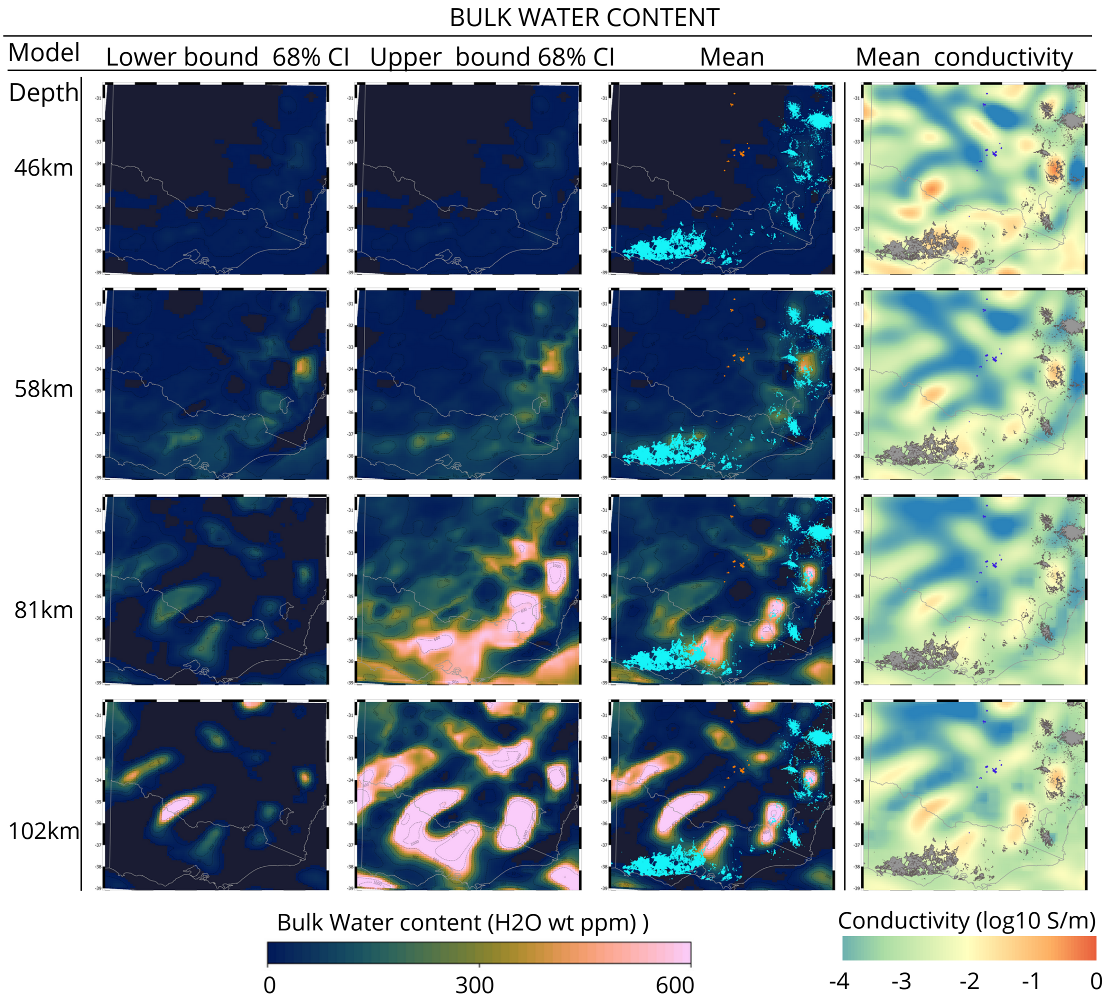

Figure 13. Bulk water content and mantle conductivity models from the joint probabilistic inversion. Columns (1)-(3): water content maps obtained from the (1) the lower, (2) upper bound of the 68% CI and (3) mean conductivity models. Column (4): depth slices from mean conductivity models of the posterior PDF. The location of leucitite- bearing volcanism and basaltic volcanoes are shown in orange and turquoise in (3); and blue and in grey in (4). Selected depths are shown on the left of the figure.

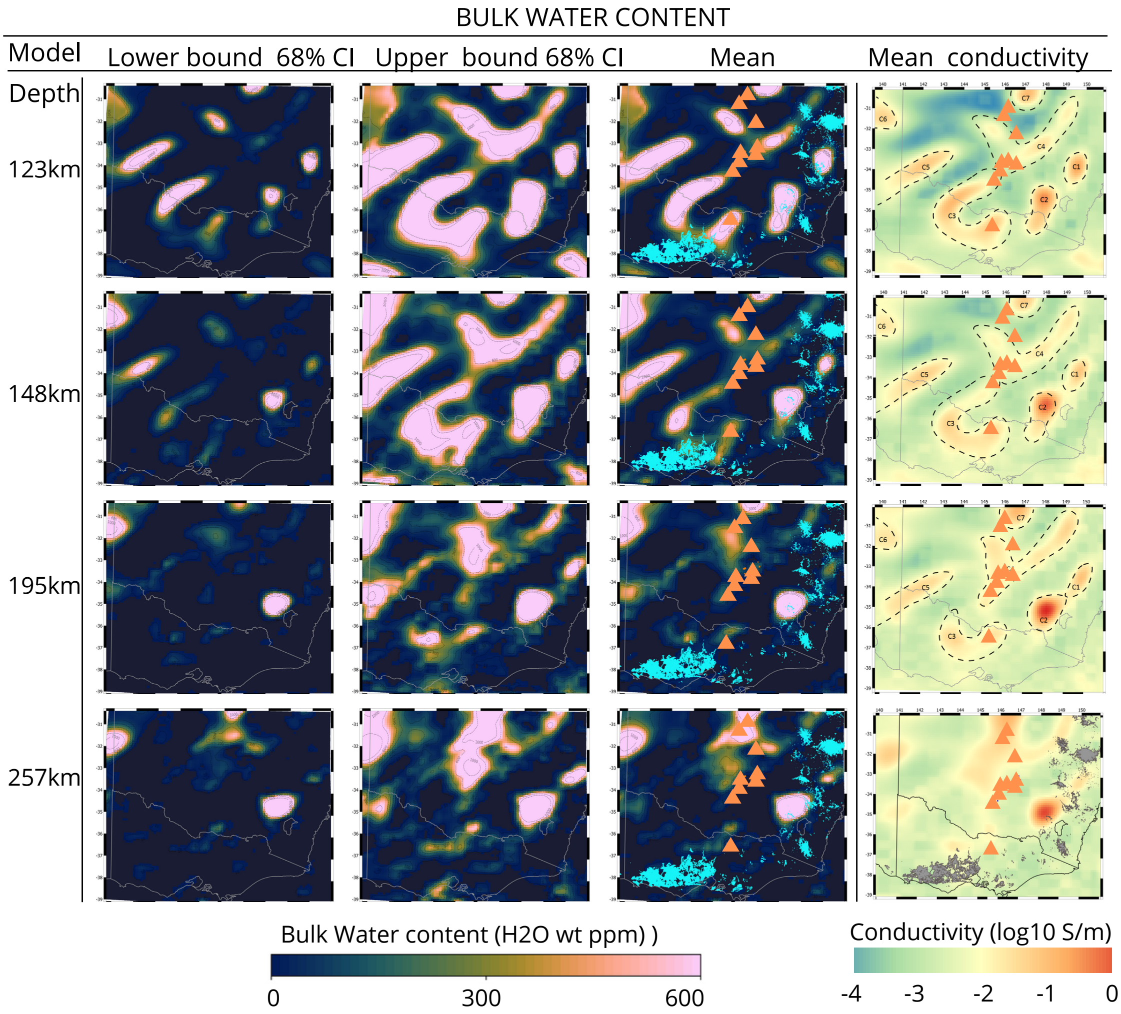

Figure 14. Bulk water content and mantle conductivity models from the joint probabilistic inversion. Columns (1)-(3): water content maps obtained from the (1) the lower, (2) upper bound of the 68% CI and (3) mean conductivity models. Column (4): depth slices from mean conductivity models of the posterior PDF. The location of leucitite- bearing volcanism and basaltic volcanoes are shown in orange and turquoise in (3); and orange and in grey in (4). We refer to the main text for an explanation of structures C1-C7 Selected depths are shown on the left of the figure.

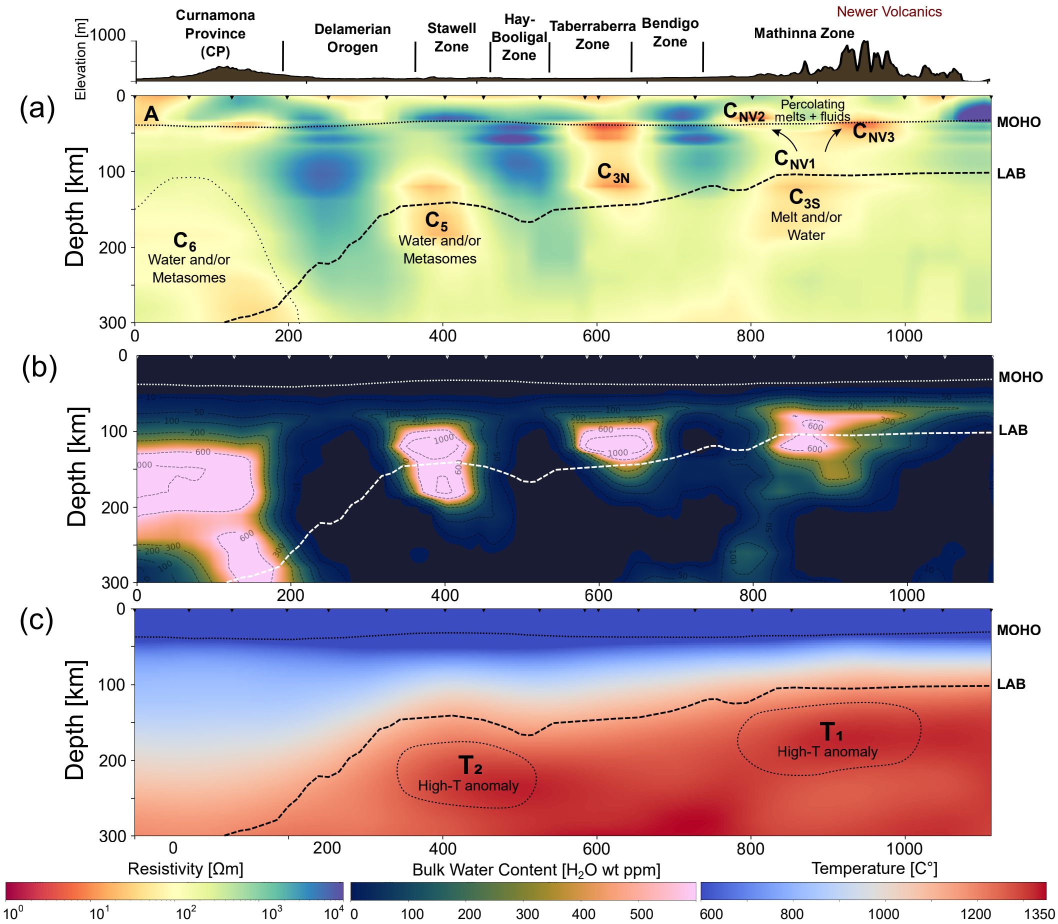

Figure 15. Vertical slices along transect A-A' (crossing most of the geological provinces) of a) the mean conductivity model, b) bulk water content derived from the mean conductivity mode and c) temperature. The Moho and LAB depths along that transect are shown in dashed lines in all panels. The elevation and location of the geological provinces is shown at the top of the figure.

The north-south transects in Figure 16 show a bulge and two defined steps in the lithospheric structure at $\sim$ 50, $\sim$ 300 and $\sim$ 650 km close to where the northern and central leucitites, and basaltic volcanoes erupted on the surface, respectively. These features in the LAB correlate with the location of sub-lithospheric high-conductivity regions (C_7, C_4 and C_{3S}). Comparing the conductivity, bulk water, and thermal structure, we observe that while the water content at C_7 and C_4 is likely to be large, C_{3S} correlates with a semi-hydrated to dry mantle region. We also observe that the conductivity of C_{3S} can be explained by the high anomalous temperatures found in that region (T_1).

Figures 17, with transects across the eastern basaltic volcanoes and the NV, show the continuation of the structure C_{3S} beneath the NV. A high-conductivity and wet region (C_1) is observed in the sub-lithospheric mantle below the Eastern Province. This deep, wet structure is also seen in Figure S6 (Supplementary material) and correlates with a high-temperature anomaly (T_3). A discussion regarding the relationship between water content, metasomatism and interpretation of the lithospheric structures described in this section is given below.

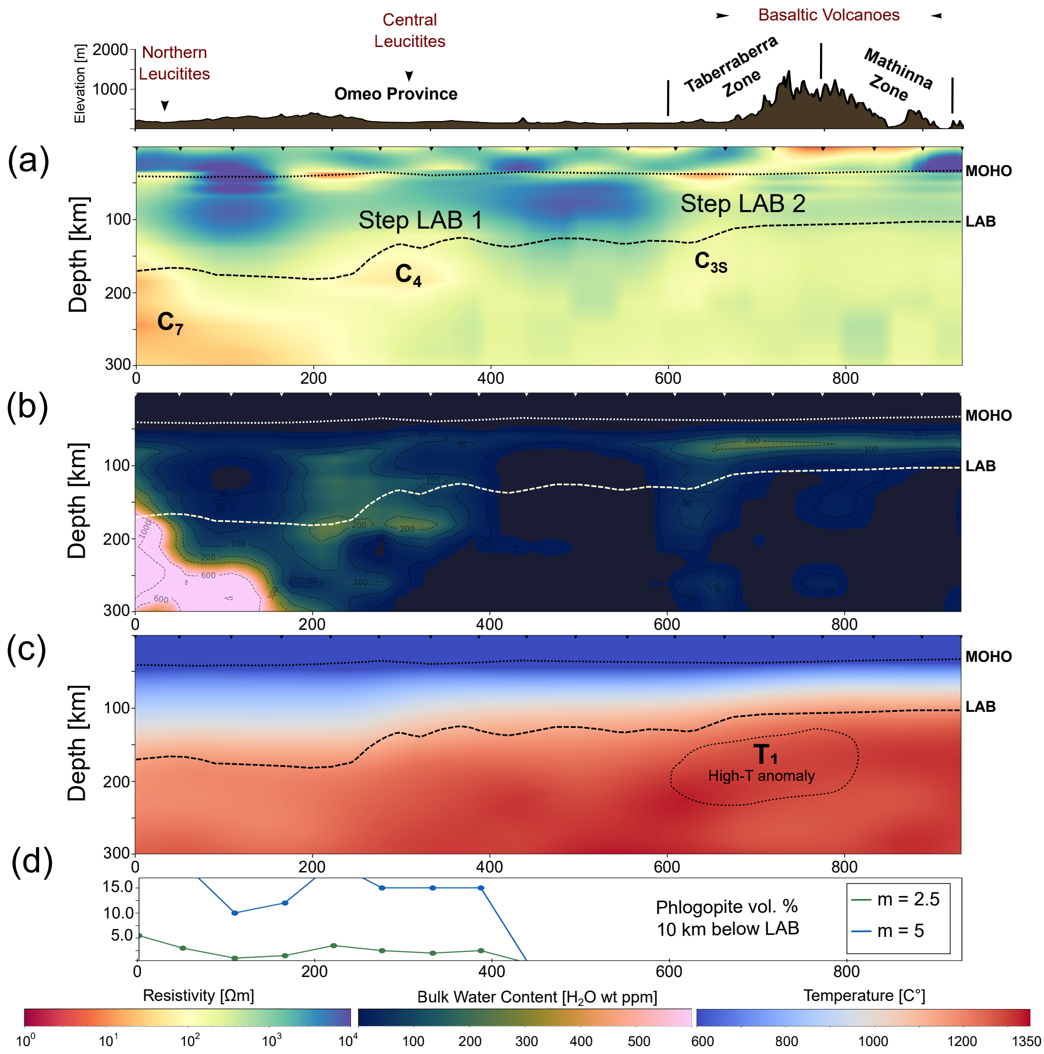

Figure 16. Vertical slices along transect D-A' (crossing the leucitite volcanics and basaltic volcanics in the south) of a) the mean conductivity model, b) bulk water content derived from the mean conductivity model and c) temperature. The Moho and LAB depths along that transect are shown in dashed lines in all panels. d) Intermediately connected (m=2.5 in blue) and poorly connected (m =5 in green) phlogopite in a dry lherzolitic matrix that fit the observed conductivities along the transect. The elevation and location of the volcanics and the NV are shown at the top of the figure.

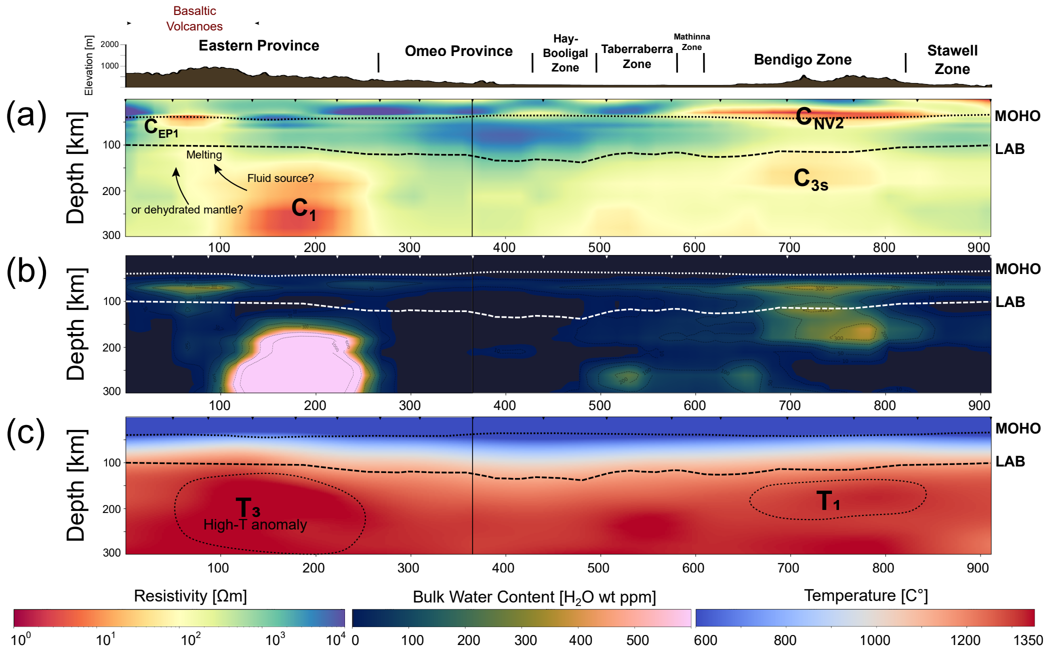

Figure 17. Vertical slices along transect B"-B'-B (across the basaltic volcanoes on the east and the NV) of a) the mean conductivity model, b) bulk water content derived from the mean conductivity model and c) temperature. The Moho and LAB depths along that transect are shown in dashed lines in all panels. The LAB depth along that transect is shown in dashed-black line in all panels. The elevation and location of the volcanics and the NV are shown at the top of the figure.

5 Discussion

5.1 Mantle metasomatism and lithospheric structure

Mantle metasomatism occurs when incipient melts or fluids react with mantle rocks. These reactions can impart chemical enrichments or alter the modal mineralogy of a mantle domain. The latter i) affect the modal proportions of peridotites, ii) introduce new volatile-bearing phases (phlogopite, amphibole, apatite, and carbonates) and, in some pervasive cases, iii) create new lithological domains, such as pyroxenite ± volatile-bearing phase lithologies (e.g. O'Reilly & Griffin, 1987). The generation of volatile-bearing phases reduces the solidus temperature (Foley et al., 2009; Pintér et al., 2021a) and increases the electrical conductivity of the mantle domain (Selway, 2014).

The bulk water content we report in this study acts as a general proxy for metasomatism or mantle fertility, i.e., the inclusion of phases (metasomes) that increase the electrical conductivity of the mantle. This proxy indicates, for example, i) the presence of water and/or phases such as graphite or sulphides for depths above 75-120 km (Selway, 2014; Özaydın & Selway, 2020); ii) co-existing water and phlogopite in cold mantle below 75-120 km depth; or iii) presence of melt in regions of elevated temperatures (via the joint assessment of bulk water content and temperature models).

5.1.1 Metasomatism across Tasmanides

Figures 15.a-b demonstrate consistent southeastward dipping lithospheric-scale structures from CP to Bendigo Zone, which correlate well with the limits of the geological provinces. We observe a successive alternation of conductive/wet and resistive/dry lithospheres that resemble the west-to-east subduction-accretion process in eastern Australia (Glen, 2005; Shea et al., 2022). The joint assessment of the transects in Figure 15 suggests that the hydrated and cold region C_6 is likely subjected to pervasive mantle metasomatism. This result is consistent with the accretion process in the area, whereby successive subduction and orogenic events introduced material into the mantle to act as metasomatic agents and, overtime, preferentially metasomatized the old, thick lithosphere.

The crustal conductor (A) below CP (described in Section 4.3.1) can be seen in Figure 15a. Kay et al. (2022) interpreted this region as deposition of interconnected graphite, which either stems from a shallow/crustal biotic source from tectonic imbrication or an abiotic source related to ascending fluids from a metasomatized mantle. We observe that the deep metasomatized mantle below CP shown in our results provides evidence to explain an abiotic source for the shallow crustal conductors. Moreover, an abiotic source could provide the mantle source reservoir for the unique heavy δC^{13} eastern Australian Group B alluvial diamonds from the Wellington field and Bingara, New South Wales (Davies et al., 2002).

5.1.2 Metasomatism below leucitite volcanoes

The leucitite lavas have melt compositions comparable to lamproites, and were derived from atypical mantle assemblage of phlogopite bearing pyroxenite (Shea et al., 2022). Due to these lava compositions, Kirkby et al. (2020) interpreted the conductors beneath the central leucitites as phlogopite stored in the mantle, suggesting a metasomatized and volatile-rich mantle region. Given the high conductivities ($< 100\Omega$ m) and bulk water content (~ 200 ppm) observed around C_4 (Figures 16), our results indicate a high probability for the presence of volatile-bearing minerals, likely introduced via modal mantle metasomatism.

Using the water calculation setup described in Section 3.5 and the phlogopite conductivity model of Li et al. (2017), we calculated the electrical conductivities of lherzolite with 5 and 10 % vol. of 0.52 w.t. fluorine-bearing phlogopite (average fluorine value of mantle rocks, Özaydın et al., 2022) for both perfectly connected (m = 1.1, Modified Archie's Law) and sparsely populated phlogopites (m = 6, Modified Archie's Law). The results show that perfectly connected cases are 2.5 orders of magnitude more conductive than the observed conductivities in the region, while the conductivity for sparsely populated/disconnected cases lay near the lower bound of the observed conductivities (Figure S7). These results suggest that a lherzolite with 5-10 % vol of intermediately connected ($6 < m < 1.1$) phlogopite explains the conductivities in C_4. Furthermore, leucitite melting from a hydrous pyroxenite source could exhaust phlogopites in the assemblage (Foley et al., 2022). If past melts have destroyed phlogopites from the source region, the residue would be reminiscent of an enriched and hydrated lherzolite (Green, 2015). Since the water content for a residual hydrous lherzolite (Green, 2015) matches with the observed bulk water content in region C_4, we conclude that the most applicable explanation for the high conductivities observed in C_4 is a hydrous lherzolite with small percentages of intermediately interconnected to sparsely populated phlogopite. These results are also illustrated in Figure 16.d , which shows the percentage of intermediately connected (m=2.5) phlogopite that can explain the observed conductivities across the leucitites volcanoes. Since large volume of phlogopite would drastically lower the seismic velocities (e.g., Selway et al., 2015) and this is not seen in our models, we note that the large percentages ($\geq 15\%$) of poorly connected (m=5) phlogopites are unlikely to explain the conductivities in the region.

The northern leucitites sit above a high-conductivity and metasomatized region below the LAB (C_7). The ultrapotassic compositions of these lavas suggest lower-degree partial melting (Cundari, 1973) which is consistent with the colder temperatures found in the region. Furthermore, potassium-rich magmas are produced by melting of a metasomatized mantle source that has been enriched in phlogopite (Xu et al., 2017; Förster et al., 2019). We calculated the effect of phlogopites in this region and found similar results to those for the central leucitite (Figures 16.d and S6) favoring intermediately connected phlogopites. The higher conductivities and colder temperature in this region compared to the central leucitites provide a favorable scenario for the presence of existing phlogopites that survived previous melting events.

5.1.3 Metasomatism underneath Newer Volcanics

The lithospheric step at ~ 650 km in Figures 16 sits below the basaltic volcanoes. This step is also seen in Figure 15 and correlates with the sub-lithospheric conductor C_{3S} and a high temperature anomaly of $\sim$1350-1400^oC (T_1). From the low-velocities observed at 60-80 km beneath the NV (Figure 5), Rawlinson et al. (2017) interpreted this temperature anomaly as a mantle upwelling and the source of the NV (see also Rawlinson et al., 2015). The existence of shallow mantle upwellings beneath lava field volcanism provides a favorable setting for decompression melting and mantle metasomatism (Aivazpourporgou et al., 2015).

In order to assess the existence of current melting in the region, we calculated water-depressed solidus curves (Hirschmann et al., 2009) for four cases of melt with the observed conductivities, temperatures and bulk water content in the lithospheric column beneath NV (Figure S8 in Supplementary Material). These four cases have melt mass fractions (Φ) and Generalised Archie's Law cementation component (m) of: (I) $\Phi = 1\%$, m = 6; (II) $\Phi = 1\%$, m = 1.1; (III) $\Phi = 10\%$, m = 6; (IV) $\Phi = 10\%$, m = 6. For the calculations we used the melt electrical conductivity model of Sifré et al. (2014), water-partitioning coefficients between melt and minerals for garnets from Novella et al. (2014) and the coefficients from Hirschmann et al. (2009) for olivine and pyroxenes. The results indicate that the geotherm in the region is not hot enough to maintain melt generation with the water content observed at C_{3S} only. However, melt can be maintained through the assimilation of carbon-bearing species and an oxidised solidus (Pintér et al., 2021b). Carbonate-bearing xenoliths entrained in lavas from NV show strong evidence for carbonatite metasomatism in the source (Yaxley et al., 1991, 1998) and could indicate presence of melt and incipient metasomatic agents (Frey et al., 1978) in the region.

We interpret that conductive metasomatic agents that percolated from C_{3S} and then C_{NV1} are a feasible explanation for the high conductivity values observed in the conductors C_{NV2} and C_{NV3} found at ~20-75 km depth beneath the basaltic volcanoes (Figure 15). This finding is consistent with the work of Shea et al. (2022) which shows that the compositions of these basalts cannot be produced by melting a garnet lherzolite mantle source, instead requiring modally metasomatized mantle sources of enriched mantle, likely pyroxenites ± hydrous phases (Frey et al., 1978; O'Reilly & Zhang, 1995; Zhang et al., 2001; Zhang & O'Reilly, 1997). This interpretation is further supported by extensive sampling of metasomatized xenoliths, including carbonate-, phlogopite-, pargasite-, and apatite-bearing samples found throughout the Newer Volcanics (Frey & Green, 1974; Yaxley et al., 1991, 1998; Bonadiman et al., 2021; Lu et al., 2020).

5.1.4 Metasomatism beneath Eastern basaltic volcanics

Beneath the volcanics of the Eastern Province, we observe highly-metasomatized sub-lithospheric regions (C_1 and C_4) and shallow conductors (C_{EP1}, C_{EP2}, C_{EP3}) at ~ 50 km depth (Figures 17 and S6). The conductor C_1 correlates with a deep temperature anomaly T_3 and a low-velocity anomaly (Figures 5). Rawlinson et al. (2015) has interpreted this velocity anomaly as the mantle source for the eastern basaltic volcanoes. Following the procedure describe above, we evaluate the existence of melt in this region (Figures S9) for melt mass fractions $\Phi = 0.25\%$ and $\Phi = 1\%$ using highly interconnected (Tubes model, Ten Grotenhuis et al., 2005) and unconnected (H-S bounds, Glover et al., 2000) melt models. The results indicate that the temperatures in T_3 are not hot enough to maintain melt only with water in the system. However, the geotherm might be just hot enough to produce some percentage of melt in combination with water and carbon-reduced solidus. If melting exist, it could be low-degree volatile-rich incipient melts that are acting as metasomatic agents; which, may be producing metasomatized mantle domains to act as sources for future major melting events (Shea et al., 2022).

Figure 18 demonstrates the relationship between the location of volcanics in the Eastern Province, the distribution of shallow conductors (average conductance 20-50 km) and mantle metasomatism (through average water content near the LAB). According to these results, basalt fields tend to be associated with shallow conductors (Figure 18a) and a dryer lithosphere (Figure 18b). Basalts also tend to surround the most metasomatized/conductive regions of the lithosphere, similar to what has been observed with kimberlites worldwide (Özaydın & Selway, 2022). Furthermore, the clear association with the distribution of lavas and shallow conductors indicate that the lavas sourced from deep mantle and traversed towards the crust. On their ascend, the lavas precipitated conductive minerals forming shallow conductors (C_{EP1}, C_{EP2}, C_{EP3} in Figures 17 and S6). Figure 17 shows a clear conductive pathway from C_1 to C_{EP1}, while the mantle beneath the volcanics is relatively dry. This dry mantle beneath the lava fields may indicate that the high-degree melting events may have exhausted the mantle source region in metasomes and water. Another possibility is that basaltic lavas were sourced from adjacent conductive/metasomatic mantle regions (C_1 and C_4) via oblique trans-lithospheric weakness zones. Further analysis with contributions from geodynamic modeling, seismic tomography and melt modeling may be required to understand the full-scope behind the genesis of melts and their structural control towards the surface in Eastern Australia.

5.2 Implications for magma generation beneath eastern Australia

Age-progressive volcanism in the EAVP, particularly along the Cosgrove track (Davies et al., 2015), has been widely attributed to mantle plume activity (Wellman & McDougall, 1974). However, Shea et al. (2022) shows primitive melt compositions throughout the

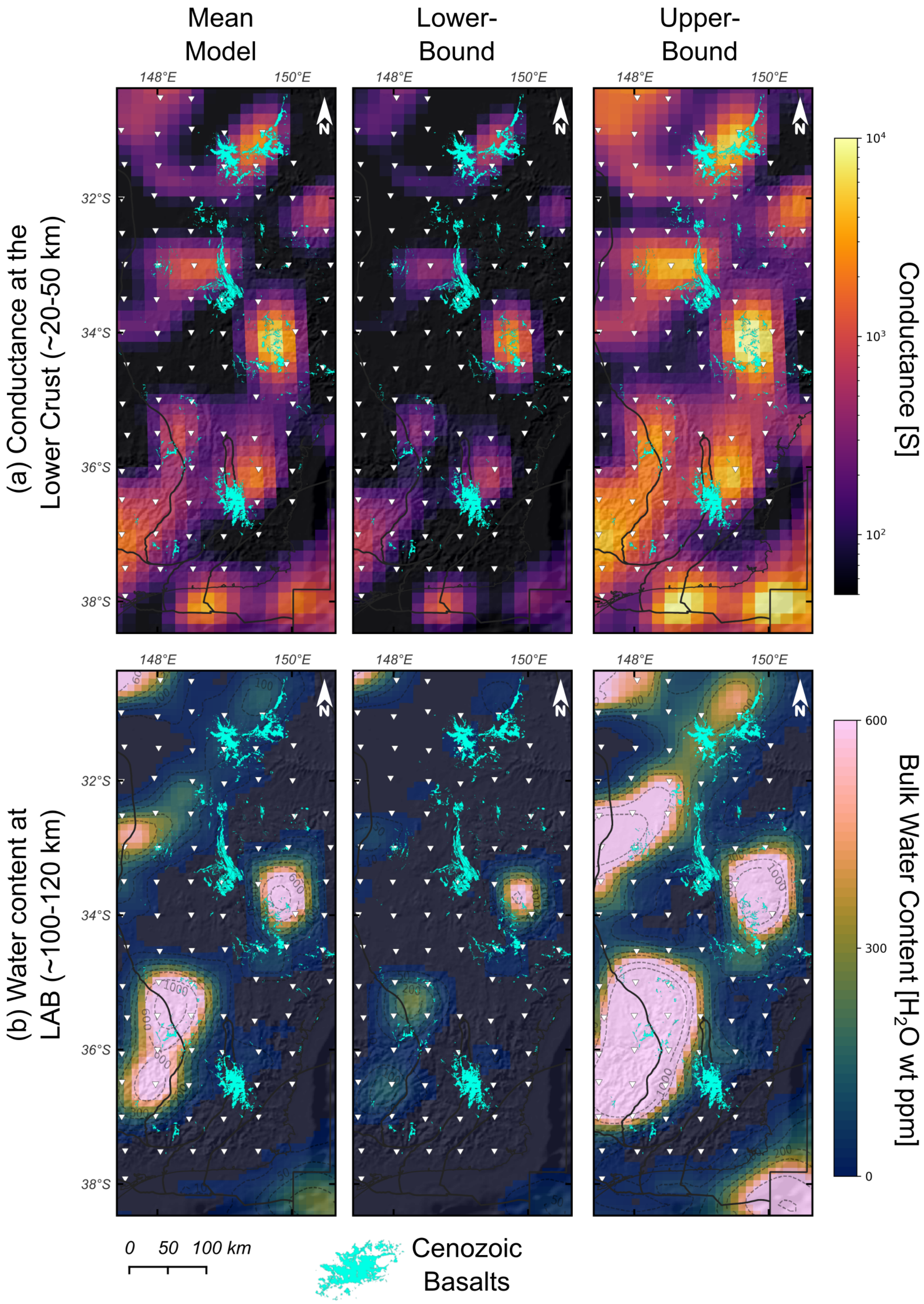

Figure 18. Relationship between Cenozoic Basalts and the parameters derived from the electrical conductivity model: (a) Conductance of the lower-crust ($\sim$ 20 − 50 km), (b) water content calculated around the LAB depth ($\sim 100 - 120$ km).

EAVP, including all age-progressive volcanism, can only be produced by melting metasomatized mantle source assemblages such as pyroxenites ± hydrous phases (amphibole and phlogopite) ± Ti-bearing oxides ± apatite. These melt compositions do not show much and mostly have no input from melting of deeper peridotite assemblages. This situation suggests that melt generation temperatures are too low to be driven by mantle plume activity.

The solidi for metasomatized mantle assemblages are $\sim 300°$C lower than anhydrous peridotites, due to their high volatile concentrations stored in hydrous minerals. In this way, melting metasomatized assemblages can produce realistic melt fractions with only slight perturbations above ambient upper mantle temperatures ($\sim 1350°$C). Furthermore, the models of Duvernay et al. (2021a) show that shear-driven upwelling (SDU) and edge-driven convection (EDC) processes that account for water content in the upper mantle at $\sim 1350^{o}C$ can produce enough melt to explain the total melt volume in the EAVP. This scenario, combined with the imaged metasomatized mantle regions, suggest that EDC and SDU are the dominant melting mechanism in eastern Australia rather than mantle plume activity (Davies & Rawlinson, 2014; Duvernay et al., 2021b; Shea et al., 2022).

Our results show a series of steps in the LAB that correlate well with both the location of basaltic and leucitites volcanoes (Figures 16 and 19). With the Australian lithospheric plate moving northeast, these steps constitute areas prone to generating sublithospheric small-scale, EDC instabilities (e.g., Zlotnik et al., 2008; Van Wijk et al., 2010; Davies & Rawlinson, 2014; Ballmer et al., 2011; Afonso et al., 2008). A 3D rendering view of these LAB steps, mean conductivity and temperature models is shown in Figure 19. This figure illustrates the proposed model for melt generation in southeastern Australia. The motion of the Australian plate creates an asthenospheric flow towards the southeast which forms an EDC-cell when it encounters a step in the LAB (above C_4 and (C_{3S}). This mantle flow detaches metasomatized lithologies from thick, older lithosphere and drags it into places where EDC occur. The metasomatic lithologies within the EDC-cell act reducing the solidus and contribute to primary metasomatized melt sources. The incipient melt produced at the EDC-cell reacts with the overlying portion of the LAB to create the source of the leucitites volcanoes.

Given the continuous displacement of the Australian plate, if one assumes the EDC as a regenerative process the question that arises is why the EDC is not generating melt continuously? We argued that the metasomatism regions act as a fusible for melt generation. Once the metasomatic lithologies (linked to the orogenic accretion) enter the cell they deplete and the melt generation stops. The residual of this process (hydrous phases) will most likely emplace in neighbouring regions. The importance of the conductivity and water content models obtained in the joint probabilistic inversion is that they are imaging the residue of these interactions rather than the actual source of the Cenozoic volcanoes. Since numerical simulations show that EDC are normally unstable and transitory, small perturbations in the sub-lithospheric mantle such as sudden acceleration of plate motion could produce new EDCs. The production of melt is likely to start when the EDC develops close to "new" metasomatized region in the lithosphere.

6 Conclusions

The results presented here demonstrate the feasibility, benefits and performance of our probabilistic approach for imaging the thermochemical structure of the lithosphere. The joint probabilistic inversion of 3D magnetotellurics (MT) and seismic data helps unlock the full potential of the MT method by providing meaningful interpretations to the conductivity anomalies and opens up new avenues for investigating metasomatism and tectono-magmatic systems. In particular, our methodology:

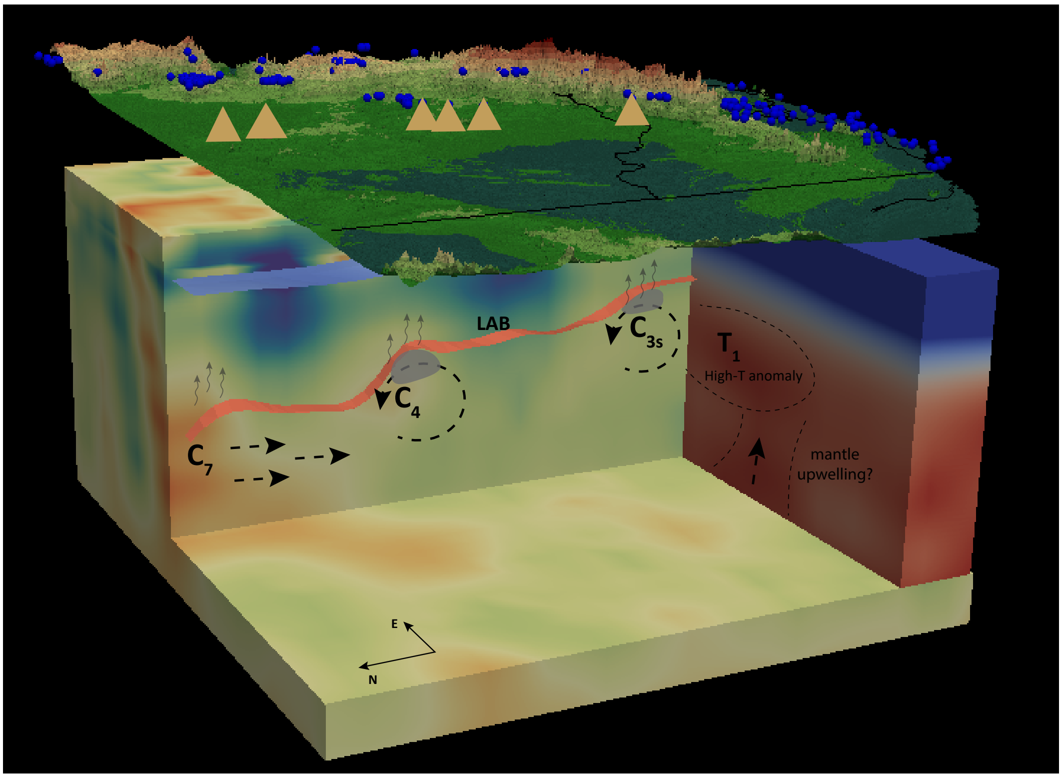

Figure 19. A 3D rendering view of these LAB steps, mean conductivity and temperature models depicting interactions between mantle metasomatism and steps in the LAB (red surface). Dashed black arrows show the flow of the asthenosphere and shearing of enriched mantle material into EDC-cells. Hotspots along the LAB are indicated by grey blobs, and locally occur where enriched mantle material crosses its solidus in the sub-lithospheric mantle. Incipient melts (grey arrows) may also travel along the LAB from deep to shallow portions of the lithospheric mantle.

- Succeeded in imaging electrical conductivity, seismic velocity, and temperature structures also identified by independent studies (Kirkby et al., 2020; Rawlinson et al., 2017; Davies et al., 2015; Pilia et al., 2015, cf.), gravity and magnetic data in the region (Nakamura & Milligan, 2015; Nakamura, 2016);
- Deals with the non-uniqueness of the MT problem and provides quantitative information on model uncertainties via well-behaved posterior distributions. This information is crucial for constraining the factors affecting the electrical conductivity. Depending the geological setting, the uncertainty in conductivity can be linked to uncertainties in temperature, partial melt or bulk water content.
- Offers an improved integrated model of the lithosphere beneath southeast Australia, which is compatible with both MT and seismic data as well as geochemical information from xenoliths. The results show improved resolution of the lithosphere-asthenospheric boundary depths and mantle electrical conductivities due to the favorable constraint of the seismic data to the thermal structure in the joint probabilistic inversion.

This study images a highly heterogeneous lithosphere beneath eastern Australia and provides insights for geodynamic and tectono-magmatic processes across multiple scales. The main takeaways that stem from our analysis can be summarised as:

- Widespread mantle metasomatism is identified throughout the region, suggesting complex interactions in the asthenosphere-lithosphere system.
- An alternation of conductive/wet and resistive/dry lithospheres that correlates with the location of geological provinces, resembling the west-to-east subduction-accretion process in eastern Australia.
- Associations between the lithospheric structure, metasomatized regions and distribution of magmatism within the Eastern Australian Volcanic Province (EAVP) are observed. For instance, high correlations are seen between the metasomatized mantle and the location of leucitite and basaltic volcanic centers. The high conductivities observed below the leucitite volcanoes indicate a residual hydrous lherzolite with small percentages of intermediately interconnected to sparsely populated phlogopite.
- The conductivities and temperature found beneath the Newer Volcanics suggest that melt maintained through the assimilation of carbon-bearing phases can exist in the region. This interpretation is supported by samples of metasomatized xenoliths throughout the EAVP.
- A series of steps in the present-day thermal structure correlate with the location of volcanic centers and constitute areas prone to develop small-scale edge-driven convection (EDC) cells in the sub-lithospheric mantle. These results, together with the petrology and melt chemistry presented in Shea et al. (2022), suggest that localised EDC processes are likely to account for the volcanism along the age-progressive tracks in EAVP, rather than a hot mantle plume (Davies et al., 2015; Kirkby et al., 2020).

Appendix A Sampling Strategy

The sampling strategy is specifically tailored to take advantage of the differential sensitivities of the seismic and MT data sets to the background and anomalous structures of the lithosphere (see Manassero et al., 2021). With this in mind, we subdivided the MCMC simulation into three main searches. The first search uses the column-based parameterization only to constrain the background conductivity and seismic velocities associated with the first-order temperature structure and large thermal anomalies. At each MCMC step, new models are obtained by randomly choosing a column and sampling all the column-parameters from their proposal distributions (Gaussian distributions centered in the current sample). The prior for the LABs are uniform distributions defined in a wide range ($60 < LAB < 320$ km) to include most of the variability that exists in continental settings (e.g. Griffin et al., 2009; Pasyanos, 2010; Fishwick, 2010; Hasterok & Chapman, 2011; Afonso et al., 2013a, and references therein). The same type of distributions are used for the thermal nodes and V_P velocities in crustal layers with bounds $400-1600^oC$ and 2-6.5 km/s, respectively. The second search focuses on constraining the conductivity anomalies that do not depend on thermo-physical state by sampling the conductivity nodes while still allowing the sampling of the column-parameters. At each MCMC iteration, the algorithm randomly chooses a type of parameter to sample (i.e. column or nodes). If a column is selected, the sampling strategy corresponds to that of the first search, otherwise the algorithm randomly chooses n nodes at a time and assigns a conductivity value from its proposal distribution (log-normal distributions). The prior for the conductivity nodes are Gaussian distributions centered on the background conductivity value (in log-scale) and standard deviation 2 $log_{10}(S/m)$. This range is large enough to keep the search as general as possible and to include most of the anomalous conductivity over the background. For a new set of nodes' values, only the 3D conductivity model is updated via interpolation using kriging (Appendix C) and its likelihood is only evaluated with the 3D MT forward solution. After these stages, the proposal distributions are adapted to multi-dimensional Gaussian and log-normal distributions for the column-parameters and the node-parameters, respectively, via the AM algorithm. At each MCMC step of the this third stage, a *metropolized independence sampler* randomly selects to sample N_{col} columns or N_{nodes} nodes.

Using prior information from previous inversions in eastern Australia, the initial 3D model (i.e., starting point) of our MCMC simulation is constructed by assembling the LAB depths for each 1D column from the model of Rawlinson et al. (2017) The crustal layers' RHP are obtained with a previous 1D joint probabilistic inversion (Haynes et al., 2020; Afonso et al., 2013a, 2013b). The initial V_P for the crustal layers and Moho depths (Figure 1.e) are taken from the regional AusREM model (Australian Seismological Reference Earth Model, Kennett & Salmon, 2012) and the initial value for each thermal node is derived from an adiabat between the initial LAB and the node at 410 km depth ($T_{410} = 1500^o$C). For the conductivity nodes, the initial values are computed as two orders of magnitude more resistive than the conductivity value at the nodes' location given by a previous deterministic inversion (Kirkby et al., 2020). In this work, we ran a total of 2,500,000 s MCMC steps for 15 frequencies using 2 processors(Intel(R) Xeon(R) CPU E5-2680 v3 @ 2.50GHz) per frequency. Even with modest computational resources, the inversion took 61 days with an average of 2.64 s per simulation. This represents a time reduction of $\sim$ 94% in the computation of the forward solution for this model.

Appendix B Mapping Thermochemical Parameters to Background Electrical Conductivity

The background conductivity structure is parameterized using the depth to the LAB and temperature nodes placed in the sub-lithospheric upper mantle. For this, we first discretized the 3D numerical model in M_{col} columns. Each column is made up of $n_x \times n_y \times n_z$ FE cells (forward problem discretization) and it is characterized by its own LAB depth, temperature nodes, bulk mantle composition and radioactive heat production (RHP) in the crust. The LAB depth and RHP are used to compute a lithospheric thermal profile by solving the 1D steady-state finite-element heat transfer problem in each column (Afonso, Rawlinson, et al., 2016) with Dirichlet boundary conditions at the surface ($T_0 = 10°C$) and at each LAB depth ($T_{LAB} = 1250°C$) (cf. Afonso, Moorkamp, & Fullea, 2016). We also compute a thermal profile in the asthenosphere interpolating the temperature-nodes from the LAB to the bottom of the numerical domain (410 km) and a pressure profile in the whole model using the following quadratic lithostatic-type approximation

Table B1: Parameters used to compute mantle conductivity

Phase	σ_0	σ_{0i}	a	b	c	d	e	f	ΔV	ΔH_i
Olivine	2.70	4.73	1.64	0.246	-4.85	3.26			0.68	2.31
Opx	3.0		1.90	-2.77	2.61	-1.09				
Cpx	3.25		2.07	-2.77	2.61	-1.09				
Garnet		4.96	2.60	-15.33	80.40	-194.6	202.6	-75.0		

and the density in the crust:

$$P(z) = 0.99 \times (4.4773 \times 10^{-3} z^2 + 3.2206 \times 10^4 z - 1.284278 \times 10^8) \tag{B1}$$

where P is pressure in Pa and z is depth in meters.

At each FE cell, we obtain the mineral phases in vol% and iron content (X_{Fe}) for olivine, orthopyroxene, clinopyroxene and garnet as a function of temperature and pressure in the mantle from pre-computed tables. These tables contain equilibrium assemblages and associated thermophysical properties derived by free energy minimization (Afonso et al., 2013b) for different temperature, pressures and major-oxide compositions. The electrical conductivity for each mineral phase is obtained using the following Arrhenius-type equation with parameters specified in Table B1:

$$\begin{aligned} \sigma &= \sigma_0 \exp\Big(\frac{-\Delta H(X_{Fe}, P)}{k_B T}\Big) + \sigma_{0i} \exp\Big(\frac{-\Delta H_i}{k_B T}\Big) + \sigma_p && \text{(B2a)} \\ \sigma_p &= f(C_w) \exp\Big(\frac{-\Delta H_{wet}(C_w)}{k_B T}\Big), && \text{(B2b)} \\ -\Delta H(X_{Fe}, P) &= a + bX_{Fe} + cX_{Fe}^2 + dX_{Fe}^3 + eX_{Fe}^4 + fX_{Fe}^5 + P\Delta V, && \text{(B2c)} \end{aligned}$$

where σ_0, σ_{0i} [S/m] and $f(C_w)$ are the small polaron, ionic and proton pre-exponential factors, respectively, ΔV [cm^3/mol] is the activation volume, ΔH, ΔH_i [eV] and ΔH_{wet} are activation enthalpies and X_{Fe} is the bulk Fe content in wt%.

The first term in the right-hand side of Equation B2a describes the contribution from small polaron conduction. Its activation enthalpy depends on iron content and pressure and its represented by a polynomial on X_{Fe} (Eq. B2c) plus a term that depends on pressure (the coefficients a, b, c, d, e, f are determined experimentally). The user can choose to consider the effect of the iron content in olivine and orthopyroxene or not. The second term of Equation B2a represents ionic conduction at high temperature and the third term (σ_p) represents the proton conduction due to hydrogen diffusion. $f(C_w)$ and ΔH_{wet} are functions of the water content C_w [wt%] and they are obtained from laboratory experiments (see e.g., Pommier, 2014; Jones, 2014, 2016). In this study we include the proton conduction term of Gardés et al. (2014b) for olivine and the term based on Dai & Karato (2009b) for pyroxenes. However, in scenarios where the mantle composition is barely known, we choose to work with a dry mantle and let the conductivity nodes accommodate the effect of water content. The preferred model for small polaron of dry garnet is based on Dai & Karato (2009d) whereas the iron effect is taken from Romano et al. (2006). The parameters for small polaron and ionic conduction for olivine, orthopyroxene clinopyroxene and garnet used in our inversion are summarised in Table A1. Finally, the bulk electrical conductivity corresponding to each FE cell is computed using the lower bound of the Hashin-–Shtrikman averaging scheme (Hashin & Shtrikman, 1962, 1963).

Appendix C Conductivity Nodes to Anomalous Electrical Conductivity

The conductivity structures related with smaller-scale features in the crust and over the background are parameterized with 7648 nodes sparsely located within the entire 3D volume. In order to define the location of the nodes, the numerical domain is first subdivided into horizontal layers (every two FE cells in the vertical direction) where their mid-points correspond to the vertical location of the nodes. Considering that bodies with dimensions smaller than the electromagnetic skin depth cannot be resolved by the MT data, the horizontal distance between nodes within each layer is chosen relative to the skin depth for the range of periods and apparent resistivities shown in the observed data. The nodal values are interpolated to each FE cell of the numerical domain via kriging (Gaussian process) interpolation (see e.g. Cressie, 1993; Rasmussen, 1997; Williams & Rasmussen, 1996; Omre, 1987; Gibbs & MacKay, 1997; Gibbs, 1998). The main idea of this method to predict the value of a function Z at m locations from n observations by computing average spatial weights (W). In simple kriging, these weights are derived using a known covariance function c between observations (given by the matrix K_{obs}) and between the observations and the m estimation locations (given by the covariance matrix K_{loc}):

$$W = K_{obs}^{-1} \cdot K_{loc}, \tag{C1}$$

where $K_{obs}=\begin{pmatrix} c(x_1^{obs}, x_1^{obs}) & ... & c(x_1^{obs}, x_n^{obs}) \\ ... & ... & .... \\ c(x_n^{obs}, x_1^{obs}) & ... & c(x_n^{obs}, x_n^{obs}) \end{pmatrix}$ and $K_{loc}=\begin{pmatrix} c(x_1^{obs}, x_1^{loc}) & ... & c(x_1^{obs}, x_m^{loc}) \\ ... & ... & .... \\ c(x_n^{obs}, x_1^{loc}) & ... & c(x_n^{obs}, x_m^{loc}) \end{pmatrix}$.

The interpolation (or estimated value) at the m locations is then given by $Z^{loc} = W \cdot Z^{obs}$, where Z^{obs} is the vector containing the n observations. We use a positive definite covariance function with spatially variable correlation lengths (Gibbs & MacKay, 1997; Gibbs, 1998; Manassero et al., 2021):

$$c(\mathbf{x}_m, \mathbf{x}_n) = \theta_1 \prod_l \left(\frac{2r_l(\mathbf{x}_m) r_l(\mathbf{x}_n)}{r_l^2(\mathbf{x}_m) + r_l^2(\mathbf{x}_n)} \right)^{1/2} exp\Big(- \sum_l \frac{(x_m^l - x_n^l)^2}{r_l^2(\mathbf{x}_m) + r_l^2(\mathbf{x}_n)} \Big) \tag{C2}$$

where $r_l(\mathbf{x})$ is an arbitrary parameterized function of position $\mathbf{x}$ defined in $[-1, 1]^2 \times [0, 1]$. The form of $r_l(\mathbf{x})$ as a function of the scaled coordinates (x, y, z) used in the main text is shown in Procedure 1 in Supplementary Material.

Acknowledgments

The data is available at www.github.com/manassero/Joint_Inv_SEAUS/tree/main/DATA. We kindly thank Nicholas Rawlinson and Simone Pilia for providing the seismic velocities models, and Anqi Zhang for providing interpolation subroutines. We also thank Isra Ezad for her insightful comments. MCM thanks support from an International Macquarie Research Excellence Scholarship (iMQRES). MCM and JCA acknowledge support from ARC Grant DP160103502, ARC Linkage Grant LP170100233, the ARC Centre of Excellence Core to Crust Fluids Systems (http://www.ccfs.mq.edu.au) and the center for Earth Evolution and Dynamics, Geoscience Australia and the European Space Agency via the "3D Earth - A Dynamic Living Planet". SÖ thanks the support from the Macquarie University COVID Recovery Fellowship fund and JJS was funded through ARC grant FL180100134. ST publishes with the permission of the Director of the Geological Survey of South Australia. AK and KC acknowledge the teams from GA, GSNSW, GSV, GSSA and the University of Adelaide involved in collecting the data and the support provided by individuals and communities to access the country, especially in remote and rural Australia. AK and KR publish with the permission of the CEO, Geoscience Australia. Resources from Macquarie University were used for this work.

References

Afonso, J. C., Fullea, J., Griffin, W., Yang, Y., Jones, A., Connolly, J., & O'Reilly, S. (2013a). 3-D multiobservable probabilistic inversion for the compositional and thermal structure of the lithosphere and upper mantle. I: A priori petrological information and geophysical observables. *Journal of Geophysical Research: Solid Earth*, *118*(5), 2586–2617.

Afonso, J. C., Fullea, J., Yang, Y., Connolly, J., & Jones, A. (2013b). 3-D multiobservable probabilistic inversion for the compositional and thermal structure of the lithosphere and upper mantle. II: General methodology and resolution analysis. *Journal of Geophysical Research: Solid Earth*, *118*(4), 1650–1676.

Afonso, J. C., Moorkamp, M., & Fullea, J. (2016). Imaging the lithosphere and upper mantle: Where we are at and where we are going. In N. L. M. Moorkamp P. Lelievre & A. Khan (Eds.), *Integrated imaging of the earth: Theory and applications* (pp. 191–218). John Wiley & Sons.

Afonso, J. C., Rawlinson, N., Yang, Y., Schutt, D. L., Jones, A. G., Fullea, J., & Griffin, W. L. (2016). 3-D multiobservable probabilistic inversion for the compositional and thermal structure of the lithosphere and upper mantle: III. Thermochemical tomography in the Western-Central US. *Journal of Geophysical Research: Solid Earth*, *121*(10), 7337–7370.

Afonso, J. C., Zlotnik, S., & Fernandez, M. (2008). Effects of compositional and rheological stratifications on small-scale convection under the oceans: Implications for the thickness of oceanic lithosphere and seafloor flattening. *Geophysical Research Letters*, *35*(20).

Aivazpourporgou, S., Thiel, S., Hayman, P. C., Moresi, L. N., & Heinson, G. (2015). Decompression melting driving intraplate volcanism in Australia: Evidence from magnetotelluric sounding. *Geophysical Research Letters*, *42*(2), 346–354.

Avdeeva, A., Moorkamp, M., Avdeev, D., Jegen, M., & Miensopust, M. (2015). Three-dimensional inversion of magnetotelluric impedance tensor data and full distortion matrix. *Geophysical Journal International*, *202*(1), 464–481.

Ballmer, M. D., Ito, G., Van Hunen, J., & Tackley, P. J. (2011). Spatial and temporal variability in Hawaiian hotspot volcanism induced by small-scale convection. *Nature Geoscience*, *4*(7), 457–460.

Bedrosian, P. A. (2016). Making it and breaking it in the Midwest: Continental assembly and rifting from modeling of EarthScope magnetotelluric data. *Precambrian Research*, *278*, 337–361.

Bell, D. R., Ihinger, P. D., & Rossman, G. R. (1995). Quantitative analysis of trace oh in garnet and pyroxenes. *American Mineralogist*, *80*(5-6), 465–474.

Bennington, N. L., Zhang, H., Thurber, C. H., & Bedrosian, P. A. (2015). Joint inversion of seismic and magnetotelluric data in the Parkfield Region of California using the normalized cross-gradient constraint. *Pure and Applied Geophysics*, *172*(5), 1033–1052.

Birch, W. D. (1978). Mineralogy and geochemistry of the leucitite at cosgrove, victoria. *Journal of the Geological Society of Australia*, *25*(7-8), 369–385.

Blackburn, G., Allison, G. B., & Leaney, F. W. J. (1982). Further evidence on the age of the tuff at mt gambier, south australia. *Transactions of the Royal Society of South Australia*, *106*, 163-167. Retrieved from `https://archive.org/details/TransactionsRoy106Roya/mode/2up`

Blatter, D., Naif, S., Key, K., & Ray, A. (2022). A plume origin for hydrous melt at the lithosphere–asthenosphere boundary. *Nature*, *604*(7906), 491–494.

Bonadiman, C., Brombin, V., Andreozzi, P., G.and Benna, Coltorti, M., Curetti, N., Faccini, B., ... Stagno, V. (2021). Phlogopite-pargasite coexistence in an oxygen reduced spinel-peridotite ambient. *Scientific Reports*, *11*(1), 1–17.

Boyd, F. (1989a). Compositional distinction between oceanic and cratonic lithosphere. *Earth and Planetary Science Letters*, *96*(1-2), 15–26.

Boyd, F. (1989b, 12). Compositional distinction between oceanic and cratonic lithosphere. *Earth and Planetary Science Letters*, *96*, 15-26. Retrieved from `https://linkinghub.elsevier.com/retrieve/pii/0012821X89901209` doi: 10.1016/0012-821X(89)90120-9

Brocher, T. M. (2005). Empirical relations between elastic wavespeeds and density in the Earth's crust. *Bulletin of the seismological Society of America*, *95*(6), 2081–2092.

Cayley, R. (2011). Exotic crustal block accretion to the eastern Gondwanaland margin in the Late Cambrian-Tasmania, the Selwyn Block, and implications for the Cambrian-Silurian evolution of the Ross, Delamerian, and Lachlan orogens. *Gondwana Research*, *19*(3), 628–649.

Cayley, R., & Musgrave, R. (2015). The Giant Lachlan Orocline—a powerful new predictive tool for mineral exploration under cover across eastern Australia. *Mines & Wines*, 29–38.

Champion, D. C., Brown, C., Mathews, E., Huston, D. L., & Kositcin, N. (2016). *Geodynamic synthesis of the Phanerozoic of eastern Australia.* Geoscience Australia.

Chave, A. D., & Jones, A. G. (2012). *The magnetotelluric method: Theory and practice.* Cambridge University Press.

Cline Ii, C., Faul, U., David, E., Berry, A., & Jackson, I. (2018). Redox-influenced seismic properties of upper-mantle olivine. *Nature*, *555*(7696), 355–358.

Cohen, B. E., Mark, D. F., Fallon, S. J., & Stephenson, P. J. (2017, 4). Holocene-neogene volcanism in northeastern australia: Chronology and eruption history. *Quaternary Geochronology*, *39*, 79-91. Retrieved from `https://www.sciencedirect.com/science/article/pii/S1871101416300826` doi: 10.1016/J.QUAGEO.2017.01.003

Comeau, M. J., Unsworth, M. J., Ticona, F., & Sunagua, M. (2015). Magnetotelluric images of magma distribution beneath Volcán Uturuncu, Bolivia: Implications for magma dynamics. *Geology*, *43*(3), 243–246.

Connolly, J. (2009). The geodynamic equation of state: what and how. *Geochemistry, Geophysics, Geosystems*, *10*(10).

Cordell, D., Naif, S., Troch, J., & Huber, C. (2022). Constraining magma reservoir conditions by integrating thermodynamic petrological models and bulk resistivity from magnetotellurics. *Geochemistry, Geophysics, Geosystems*, *23*(9), e2022GC010455.

Cressie, N. (1993). *Statistics for spatial data* (Revised Edition ed.). Wiley-Interscience.

Cundari, A. (1973). Petrology of the leucite-bearing lavas in New South Wales. *Journal of the Geological Society of Australia*, *20*, 465-492. Retrieved from `https://doi.org/10.1080/00167617308728829` doi: 10.1080/00167617308728829

Dai, L., & Karato, S.-i. (2009a). Electrical conductivity of orthopyroxene: Implications for the water content of the asthenosphere. *Proceedings of the Japan Academy, Series B*, *85*(10), 466–475.

Dai, L., & Karato, S.-i. (2009b). Electrical conductivity of orthopyroxene: Implications for the water content of the asthenosphere. *Proceedings of the Japan Academy, Series B*, *85*(10), 466–475.

Dai, L., & Karato, S.-i. (2009c). Electrical conductivity of pyrope-rich garnet at high temperature and high pressure. *Physics of the Earth and Planetary Interiors*, *176*(1-2), 83–88.

Dai, L., & Karato, S.-i. (2009d). Electrical conductivity of pyrope-rich garnet at high temperature and high pressure. *Physics of the Earth and Planetary Interiors*, *176*(1-2), 83–88.

Davies, O'Reilly, S., & Griffin, W. (2002). Multiple origins of alluvial diamonds from New South Wales, Australia. *Economic Geology*, *97*(1), 109–123.

Davies, & Rawlinson, N. (2014). On the origin of recent intraplate volcanism in Australia. *Geology*, *42*(12), 1031–1034.

Davies, Rawlinson, N., Iaffaldano, G., & Campbell, I. H. (2015). Lithospheric controls on magma composition along Earth's longest continental hotspot track. *Nature*, *525*(7570), 511–514.

Demidjuk, Z., Turner, S., Sandiford, M., George, R., Foden, J., & Etheridge, M. (2007). U-series isotope and geodynamic constraints on mantle melting processes beneath the Newer Volcanic Province in South Australia. *Earth and Planetary Science Letters*, *261*(3-4), 517–533.

Demouchy, S., Shcheka, S., Denis, C. M., & Thoraval, C. (2017). Subsolidus hydrogen partitioning between nominally anhydrous minerals in garnet-bearing peridotite. *American Mineralogist: Journal of Earth and Planetary Materials*, *102*(9), 1822–1831.

Duvernay, T., Davies, D. R., Mathews, C., Gibson, A., & Kramer, S. (2021b). Linking intraplate volcanism to lithospheric structure and asthenospheric flow. *Geochemistry, Geophysics, Geosystems*, *22*, 1-29. doi: 10.1029/2021GC009953

Duvernay, T., Davies, D. R., Mathews, C. R., Gibson, A. H., & Kramer, S. C. (2021a). Linking intraplate volcanism to lithospheric structure and asthenospheric flow. *Geochemistry, Geophysics, Geosystems*, *22*(8), e2021GC009953.

Evans, R. (2012). Conductivity of Earth materials. In J. A. Chave A. (Ed.), *The magnetotelluric method, theory and practice* (pp. 50–95). Cambridge: Cambridge Univ. Press New York.

Evans, R., Benoit, M. H., Long, M. D., Elsenbeck, J., Ford, H. A., Zhu, J., & Garcia, X. (2019). Thin lithosphere beneath the central Appalachian Mountains: A combined seismic and magnetotelluric study. *Earth and Planetary Science Letters*, *519*, 308–316.

Farquharson, C. G., & Oldenburg, D. W. (1998). Non-linear inversion using general measures of data misfit and model structure. *Geophysical Journal International*, *134*(1), 213–227.

Fishwick, S. (2010). Surface wave tomography: imaging of the lithosphere–asthenosphere boundary beneath central and southern Africa? *Lithos*, *120*(1-2), 63–73.

Foley, S., Ezad, I., van der Laan Sieger, & Pertermann, M. (2022, 3). Melting of hydrous pyroxenites with alkali amphiboles in the continental mantle: 1. melting relations and major element compositions of melts. *Geoscience Frontiers*, 101380. Retrieved from `https://linkinghub.elsevier.com/retrieve/pii/S1674987122000330` doi: 10.1016/j.gsf.2022.101380

Foley, S., Yaxley, G., Rosenthal, A., Buhre, S., Kiseeva, E., Rapp, R., & Jacob, D. (2009). The composition of near-solidus melts of peridotite in the presence of CO2 and H2O between 40 and 60ákbar. *Lithos*, *112*, 274–283.

Förster, M. W., Buhre, S., Xu, B., Prelević, D., Mertz-Kraus, R., & Foley, S. F. (2019). Two-stage origin of k-enrichment in ultrapotassic magmatism simulated by melting of experimentally metasomatized mantle. *Minerals*, *10*(1), 41.

Frey, F., & Green, D. (1974). The mineralogy, geochemistry and origin of iherzolite inclusions in victorian basanites. *Geochimica et Cosmochimica Acta*, *38*, 1023-1059. Retrieved from `http://www.sciencedirect.com/science/article/pii/0016703774900039` doi: https://doi.org/10.1016/0016-7037(74)90003-9

Frey, F., Green, D., & Roy, S. (1978). Integrated models of basalt petrogenesis: a study of quartz tholeiites to olivine melilitites from south eastern Australia utilizing geochemical and experimental petrological data. *Journal of petrology*, *19*(3), 463–513.

Fullea, J., Muller, M., & Jones, A. (2011). Electrical conductivity of continental lithospheric mantle from integrated geophysical and petrological modeling: Application to the Kaapvaal Craton and Rehoboth Terrane, southern Africa. *Journal of Geophysical Research: Solid Earth*, *116*(B10), 94–105. doi: doi:10.1029/2011JB008544

Gallardo, L. A., & Meju, M. A. (2007). Joint two-dimensional cross-gradient imaging of magnetotelluric and seismic traveltime data for structural and lithological classification. *Geophysical Journal International*, *169*(3), 1261–1272.

García-Yeguas, A., Ledo, J., Piña-Varas, P., Prudencio, J., Queralt, P., Marcuello, A., ... Pérez, N. (2017). A 3d joint interpretation of magnetotelluric and seismic tomographic models: The case of the volcanic island of Tenerife. *Computers & Geosciences*, *109*, 95–105.

Gardés, E., Gaillard, F., & Tarits, P. (2014a). Toward a unified hydrous olivine electrical conductivity law. *Geochemistry, Geophysics, Geosystems*, *15*(12), 4984–5000.

Gardés, E., Gaillard, F., & Tarits, P. (2014b). Toward a unified hydrous olivine electrical conductivity law. *Geochemistry, Geophysics, Geosystems*, *15*(12), 4984–5000.

Gibbs, M. (1998). *Bayesian Gaussian processes for regression and classification* (Unpublished doctoral dissertation). Citeseer.

Gibbs, M., & MacKay, D. J. (1997). Efficient implementation of Gaussian processes. *Neural Computation*.

Gilks, W. R., Richardson, S., & Spiegelhalter, D. (1995). *Markov chain Monte Carlo in practice.* Chapman and Hall/CRC.

Glen, R. (2005). The tasmanides of eastern australia. *Special Publication-Geological Society of London*, *246*, 23.

Glen, R. (2013). Refining accretionary orogen models for the Tasmanides of eastern Australia. *Australian Journal of Earth Sciences*, *60*(3), 315–370.

Glover, P. W. (2010). A generalized archie's law for n phases. *Geophysics*, *75*(6), E247–E265.

Glover, P. W., Hole, M. J., & Pous, J. (2000). A modified Archie's law for two conducting phases. *Earth and Planetary Science Letters*, *180*(3-4), 369–383.

Goes, S., Govers, R., Vacher, & P. (2000). Shallow mantle temperatures under Europe from P and S wave tomography. *Journal of Geophysical Research: Solid Earth*, *105*(B5), 11153–11169.

Green, D. H. (2015). Experimental petrology of peridotites, including effects of water and carbon on melting in the earth's upper mantle. *Physics and Chemistry of Minerals*, *42*, 95-122. doi: 10.1007/s00269-014-0729-2

Gregory, P. (2005). *Bayesian Logical Data Analysis for the Physical Sciences: A Comparative Approach with Mathematica® Support.* Cambridge University Press.

Griffin, W., Begg, G., & O'reilly, S. Y. (2013). Continental-root control on the genesis of magmatic ore deposits. *Nature Geoscience*, *6*(11), 905.

Griffin, W., O'reilly, S. Y., Afonso, J. C., & Begg, G. (2009). The composition and evolution of lithospheric mantle: a re-evaluation and its tectonic implications. *Journal of Petrology*, *50*(7), 1185–1204.

Griffin, W., Sutherland, F., & Hollis, J. (1987, 4). Geothermal profile and crust-mantle transition beneath east-central Queensland: Volcanology, xenolith petrology and seismic data. *Journal of Volcanology and Geothermal Research*, *31*, 177-203. Retrieved from `https://www.sciencedirect.com/science/article/pii/0377027387900679` doi: 10.1016/0377-0273(87)90067-9

Haario, H., Laine, M., Mira, A., & Saksman, E. (2006). DRAM: efficient adaptive MCMC. *Statistics and computing*, *16*(4), 339–354.

Hand, M. P., Reid, A. J., Szpunar, M. A., Direen, N., Wade, B., Payne, J., & Barovich, K. M. (2008). Crustal architecture during the early Mesoproterozoic Hiltaba-related mineralisation event: are the Gawler Range Volcanics a foreland basin fill? *MESA Journal*, *51*, 19–24.

Hashin, Z., & Shtrikman, S. (1962). A variational approach to the theory of the effective magnetic permeability of multiphase materials. *Journal of applied Physics*, *33*(10), 3125–3131.

Hashin, Z., & Shtrikman, S. (1963). A variational approach to the theory of the elastic behaviour of multiphase materials. *Journal of the Mechanics and Physics of Solids*, *11*(2), 127–140.

Hassani, B., & Renaudin, A. (2013). The cascade bayesian approach for a controlled integration of internal data, external data and scenarios.

Hasterok, D., & Chapman, D. (2011). Heat production and geotherms for the continental lithosphere. *Earth and Planetary Science Letters*, *307*(1-2), 59–70.

Haynes, M., Fomin, I., Afonso, J. C., Gorbatov, A., Czarnota, K., & Salajegheh, F. (2020). *Developing thermochemical models of Australia's lithosphere.* Geoscience Australia.

Heinson, G., Didana, Y., Soeffky, P., Thiel, S., & Wise, T. (2018). The crustal geophysical signature of a world-class magmatic mineral system. *Scientific reports*, *8*(1), 1–6.

Heinson, G., Duan, J., Kirkby, A., Robertson, K., Thiel, S., Aivazpourporgou, S., & Soyer, W. (2021). Lower crustal resistivity signature of an orogenic gold system. *Scientific Reports*, *11*(1), 1–7.

Hirschmann, M. M., Tenner, T., Aubaud, C., & Withers, A. (2009). Dehydration melting of nominally anhydrous mantle: The primacy of partitioning. *Physics of the Earth and Planetary Interiors*, *176*(1-2), 54–68.

Irving, A. J. (1980). Petrology and geochemistry of composite ultramafic xenoliths in alkalic basalts and implications for magmatic processes within the mantle. *American Journal of Science*, *280*, 389-416.

Jegen, M. D., Hobbs, R. W., Tarits, P., & Chave, A. (2009). Joint inversion of marine magnetotelluric and gravity data incorporating seismic constraints: Preliminary results of sub-basalt imaging off the Faroe Shelf. *Earth and Planetary Science Letters*, *282*(1-4), 47–55.

Johnson, R. W., Johnson, R. W., Knutson, J., & Taylor, S. R. (1989). *Intraplate volcanism: in eastern Australia and New Zealand.* Cambridge University Press.

Jones, A. G. (1999). Imaging the continental upper mantle using electromagnetic methods. *Lithos*, *48*(1-4), 57–80.

Jones, A. G. (2011). Three-dimensional galvanic distortion of three-dimensional regional conductivity structures: Comment on" three-dimensional joint inversion for magnetotelluric resistivity and static shift distributions in complex media" by Yutaka Sasaki and Max A. Meju. *Journal of Geophysical Research. Solid Earth*, *116*(12).

Jones, A. G. (2014). Reconciling different equations for proton conduction using the Meyer-Neldel compensation rule. *Geochemistry, Geophysics, Geosystems*, *15*(2), 337–349.

Jones, A. G. (2016). Proton conduction and hydrogen diffusion in olivine: an attempt to reconcile laboratory and field observations and implications for the role of grain boundary diffusion in enhancing conductivity. *Physics and Chemistry of Minerals*, *43*(4), 237–265.

Jones, A. G., Afonso, J. C., & Fullea, J. (2017). Geochemical and geophysical constrains on the dynamic topography of the Southern African Plateau. *Geochemistry, Geophysics, Geosystems*, *18*(10), 3556–3575.

Karato, S.-i. (1990). The role of hydrogen in the electrical conductivity of the upper mantle. *Nature*, *347*(6290), 272.

Karato, S.-i. (2006). Remote sensing of hydrogen in earth's mantle. *Reviews in Mineralogy and Geochemistry*, *62*(1), 343–375.

Kay, B., Heinson, G., & Brand, K. (2022). Crustal magnetotelluric imaging of a Paleoproterozoic graphitic suture zone, Curnamona Province, Australia. *Gondwana Research*, *106*, 1–14.

Kelbert, A., Meqbel, N., Egbert, G. D., & Tandon, K. (2014). ModEM: A modular system for inversion of electromagnetic geophysical data. *Computers & Geosciences*, *66*, 40–53.

Kennett, B., & Salmon, M. (2012). Ausrem: Australian seismological reference model. *Australian Journal of Earth Sciences*, *59*(8), 1091–1103.

Khan, A. (2016). On Earth's mantle constitution and structure from joint analysis of geophysical and laboratory-based data: An example. *Surveys in Geophysics*, *37*(1), 149–189.

Khan, A., Connolly, J., & Olsen, N. (2006). Constraining the composition and thermal state of the mantle beneath europe from inversion of long-period electromagnetic sounding data. *Journal of Geophysical Research: Solid Earth*, *111*(B10).

Kirkby, A., Czarnota, K., Huston, D. L., Champion, D. C., Doublier, M. P., Bedrosian, P. A., ... Heinson, G. (2022). Lithospheric conductors reveal source regions of convergent margin mineral systems. *Scientific Reports*, *12*(1), 1–10.

Kirkby, A., Musgrave, R. J., Czarnota, K., Doublier, M. P., Duan, J., Cayley, R. A., & Kyi, D. (2020). Lithospheric architecture of a Phanerozoic orogen from magnetotellurics: AusLAMP in the Tasmanides, southeast Australia. *Tectonophysics*, *793*, 228560.

Li, Y., Jiang, H., & Yang, X. (2017). Fluorine follows water: Effect on electrical conductivity of silicate minerals by experimental constraints from phlogopite. *Geochimica et Cosmochimica Acta*, *217*, 16–27.

Liu, H., Zhu, Q., & Yang, X. (2019). Electrical conductivity of oh-bearing omphacite and garnet in eclogite: the quantitative dependence on water content. *Contributions to Mineralogy and Petrology*, *174*(7), 1–15.

Lu, J., Griffin, W. L., Tilhac, R., Xiong, Q., Zheng, J., & O'Reilly, S. Y. (2018). Tracking deep lithospheric events with garnet-websterite xenoliths from southeastern Australia. *Journal of Petrology*, *59*(5), 901–930.

Lu, J., Tilhac, R., Griffin, W. L., Zheng, J., Xiong, Q., Oliveira, B., & O'Reilly, S. Y. (2020). Lithospheric memory of subduction in mantle pyroxenite xenoliths from rift-related basalts. *Earth and Planetary Science Letters*, *544*, 116365.

Manassero, M. C., Afonso, J. C., Zyserman, F., Jones, A., Zlotnik, S., & Fomin, I. (2021). A Reduced Order Approach for Probabilistic Inversions of 3D Magnetotelluric Data II: Joint Inversion of MT and Surface-Wave Data. *Journal of Geophysical Research: Solid Earth*, *126*(12), e2021JB021962.

Manassero, M. C., Afonso, J. C., Zyserman, F., Zlotnik, S., & Fomin, I. (2020). A Reduced Order Approach for Probabilistic Inversions of 3D Magnetotelluric Data I: General Formulation. *Geophysical Journal International*, *223*(3), 1837–1863.

McDonough, W. (1990, 11). Constraints on the composition of the continental lithospheric mantle. *Earth and Planetary Science Letters*, *101*, 1-18. Retrieved from `https://linkinghub.elsevier.com/retrieve/pii/0012821X9090119I` doi: 10.1016/0012-821X(90)90119-I

Miensopust, M. P., Queralt, P., Jones, A. G., & modellers, D. M. (2013). Magnetotelluric 3-D inversion—a review of two successful workshops on forward and inversion code testing and comparison. *Geophysical Journal International*, *193*(3), 1216–1238.

Moorkamp, M., Jones, A., & Eaton, D. (2007). Joint inversion of teleseismic receiver functions and magnetotelluric data using a genetic algorithm: Are seismic velocities and electrical conductivities compatible? *Geophysical Research Letters*, *34*(16).

Moorkamp, M., Jones, A., & Fishwick, S. (2010). Joint inversion of receiver functions, surface wave dispersion, and magnetotelluric data. *Journal of Geophysical Research: Solid Earth*, *115*(B4).

Moresi, L., Betts, P. G., Miller, M. S., & Cayley, R. A. (2014). Dynamics of continental accretion. *Nature*, *508*(7495), 245–248.

Musgrave, R. (2015). Oroclines in the Tasmanides. *Journal of Structural Geology*, *80*, 72–98.

Musgrave, R., & Rawlinson, N. (2010). Linking the upper crust to the upper mantle: comparison of teleseismic tomography with long-wavelength features of the gravity and magnetic fields of southeastern Australia. *Exploration Geophysics*, *41*(2), 155–162.

Naif, S., Selway, K., Murphy, B. S., Egbert, G., & Pommier, A. (2021). Electrical conductivity of the lithosphere-asthenosphere system. *Physics of the Earth and Planetary Interiors*, *313*(2021), 10661.

Nakamura, A. (2016). *Isostatic residual gravity anomaly grid of onshore Australia 2016.*

Nakamura, A., & Milligan, P. (2015). *Total magnetic intensity (TMI) colour composite image. Canberra: Geoscience Australia.*

Novella, D., Frost, D. J., Hauri, E. H., Bureau, H., Raepsaet, C., & Roberge, M. (2014). The distribution of h2o between silicate melt and nominally anhydrous peridotite and the onset of hydrous melting in the deep upper mantle. *Earth and Planetary Science Letters*, *400*, 1–13.

Omre, H. (1987). Bayesian kriging—merging observations and qualified guesses in kriging. *Mathematical Geology*, *19*(1), 25–39.

O'Reilly, S., & Griffin, W. (1985, 1). A xenolith-derived geotherm for southeastern australia and its geophysical implications. *Tectonophysics*, *111*, 41-63. Retrieved from `https://linkinghub.elsevier.com/retrieve/pii/0040195185900654` doi: 10.1016/0040-1951(85)90065-4

O'Reilly, S., & Griffin, W. (1987). Eastern Australia-4000 kilometres of mantle samples. In *Mantle zenoliths* (pp. 267–280). John Wiley & Sons.

Özaydın, S., & Selway, K. (2020). MATE: An analysis tool for the interpretation of magnetotelluric models of the mantle. *Geochemistry, Geophysics, Geosystems*, *21*(9), e2020GC009126.

Özaydın, S., & Selway, K. (2022). The relationship between kimberlitic magmatism and electrical conductivity anomalies in the mantle. *Geophysical Research Letters*, e2022GL099661.

Özaydın, S., Selway, K., Griffin, W. L., & Moorkamp, M. (2022). Probing the southern African lithosphere with magnetotellurics: 2. Linking electrical conductivity, composition, and tectonomagmatic evolution. *Journal of Geophysical Research: Solid Earth*, *127*(3), e2021JB023105.

O'Reilly, S. Y., & Zhang, M. (1995). Geochemical characteristics of lava-field basalts from eastern Australia and inferred sources: connections with the subcontinental lithospheric mantle? *Contributions to Mineralogy and Petrology*, *121*(2), 148–170.

Padrón-Navarta, J. A., & Hermann, J. (2017). A subsolidus olivine water solubility equation for the earth's upper mantle. *Journal of Geophysical Research: Solid Earth*, *122*(12), 9862–9880.

Page, R., Conor, C., Stevens, B., Gibson, G. M., Preiss, W. V., & Southgate, P. (2005). Correlation of Olary and Broken Hill domains, Curnamona Province: Possible relationship to Mount Isa and other North Australian Pb-Zn-Ag-bearing successions. *Economic Geology*, *100*(4), 663–676.

Pasyanos, M. E. (2010). Lithospheric thickness modeled from long-period surface wave dispersion. *Tectonophysics*, *481*(1-4), 38–50.

Pearson, N., O'Reilly, S., & Griffin, W. (1991, 6). Heterogeneity in the thermal state of the lower crust and upper mantle beneath eastern australia. *Exploration Geo-*

physics, *22*, 295-298. Retrieved from https://www.tandfonline.com/doi/full/10.1071/EG991295 doi: 10.1071/EG991295

Pilia, S., Rawlinson, N., Cayley, R., Bodin, T., Musgrave, R., Reading, A., ... Young, M. (2015). Evidence of micro-continent entrainment during crustal accretion. *Scientific reports*, *5*(1), 1–6.

Pintér, Z., Foley, S. F., Yaxley, G. M., Rosenthal, A., Rapp, R. P., Lanati, A. W., & Rushmer, T. (2021a). Experimental investigation of the composition of incipient melts in upper mantle peridotites in the presence of CO2 and H2O. *Lithos*, *396*, 106224.

Pintér, Z., Foley, S. F., Yaxley, G. M., Rosenthal, A., Rapp, R. P., Lanati, A. W., & Rushmer, T. (2021b). Experimental investigation of the composition of incipient melts in upper mantle peridotites in the presence of co2 and h2o. *Lithos*, *396*, 106224.

Pommier, A. (2014). Interpretation of magnetotelluric results using laboratory measurements. *Surveys in Geophysics*, *35*(1), 41–84.

Rasmussen, C. E. (1997). *Evaluation of Gaussian processes and other methods for non-linear regression* (Unpublished doctoral dissertation). University of Toronto Toronto, Canada.

Rawlinson, N., Davies, D., & Pilia, S. (2017). The mechanisms underpinning Cenozoic intraplate volcanism in eastern Australia: Insights from seismic tomography and geodynamic modeling. *Geophysical Research Letters*, *44*(19), 9681–9690.

Rawlinson, N., Kennett, B., Salmon, M., & Glen, R. (2015). Origin of lateral heterogeneities in the upper mantle beneath south-east Australia from seismic tomography. In *The earth's heterogeneous mantle* (pp. 47–78). Springer.

Rawlinson, N., Pilia, S., Young, M., Salmon, M., & Yang, Y. (2016). Crust and upper mantle structure beneath southeast Australia from ambient noise and teleseismic tomography. *Tectonophysics*, *689*, 143–156.

Raymond, O., Liu, S., Gallagher, R., Zhang, W., & Highet, L. (2012). Surface geology of Australia 1: 1 million scale dataset 2012 edition. *Geoscience Australia, Canberra*.

Raymond, O., Totterdell, J., Stewart, A., & Woods, M. (2018). Australian Geological Provinces, 2018. *Geoscience Australia, Canberra*.

Ringwood, A. E. (1962, 2). A model for the upper mantle. *Journal of Geophysical Research*, *67*, 857-867. doi: 10.1029/JZ067i002p00857

Robertson, K., Heinson, G., & Thiel, S. (2016). Lithospheric reworking at the Proterozoic–Phanerozoic transition of Australia imaged using AusLAMP Magnetotelluric data. *Earth and Planetary Science Letters*, *452*, 27–35.

Romano, C., Poe, B. T., Kreidie, N., & McCammon, C. A. (2006). Electrical conductivities of pyrope-almandine garnets up to 19 GPa and 1700 C. *American Mineralogist*, *91*(8-9), 1371–1377.

Rosas-Carbajal, M., Linde, N., Kalscheuer, T., & Vrugt, J. A. (2013). Two-dimensional probabilistic inversion of plane-wave electromagnetic data: methodology, model constraints and joint inversion with electrical resistivity data. *Geophysical Journal International*, *196*(3), 1508–1524.

Rosenbaum, G. (2018). The Tasmanides: Phanerozoic tectonic evolution of eastern Australia. *Annual Review of Earth and Planetary Sciences*, *46*, 291–325.

Selway, K. (2014). On the causes of electrical conductivity anomalies in tectonically stable lithosphere. *Surveys in Geophysics*, *35*(1), 219–257.

Selway, K., Ford, H., & Kelemen, P. (2015). The seismic mid-lithosphere discontinuity. *Earth and Planetary Science Letters*, *414*, 45–57.

Selway, K., & O'Donnell, J. (2019). A small, unextractable melt fraction as the cause for the low velocity zone. *Earth and Planetary Science Letters*, *517*, 117–124.

Shea, J. J., Ezad, I. S., Foley, S. F., & Lanati, A. W. (2022, 8). The eastern australian volcanic province, its primitive melts, constraints on melt sources and the influence of mantle metasomatism. *Earth-Science Reviews*, 104168. Retrieved from `https://linkinghub.elsevier.com/retrieve/pii/S0012825222002525` doi: 10.1016/j.earscirev.2022.104168

Sifré, D., Gardés, E., Massuyeau, M., Hashim, L., Hier-Majumder, S., & Gaillard, F. (2014, May). Electrical conductivity during incipient melting in the oceanic low-velocity zone. *Nature*, *509*(7498), 81–85. Retrieved 2022-04-27, from `http://www.nature.com/articles/nature13245` doi: 10.1038/nature13245

Smith, B. W., & Prescott, J. R. (1987). Thermoluminescence dating of the eruption at mt schank, south australia. *Australian Journal of Earth Sciences*, *34*, 335-342. doi: 10.1080/08120098708729415

Snyder, D., Hillier, M., Kjarsgaard, B., De Kemp, E., & Craven, J. (2014). Lithospheric architecture of the Slave craton, northwest Canada, as determined from an interdisciplinary 3-D model. *Geochemistry, Geophysics, Geosystems*, *15*(5), 1895–1910.

Stixrude, L., & Lithgow-Bertelloni, C. (2011). Thermodynamics of mantle minerals-ii. phase equilibria. *Geophysical Journal International*, *184*(3), 1180–1213.

Sutherland, F., Graham, I., Meffre, S., Zwingmann, H., & Pogson, R. (2012). Passive-margin prolonged volcanism, East Australian Plate: outbursts, progressions, plate controls and suggested causes. *Australian Journal of Earth Sciences*, *59*(7), 983–1005.

Sutherland, F., Raynor, L., & Pogson, R. (1994). Spinel to garnet lherzolite transition in relation to high temperature palaeogeotherms, eastern australia. *Australian Journal of Earth Sciences*, *41*, 205-220. doi: 10.1080/08120099408728130

Takam Takougang, E. M., Harris, B., Kepic, A., & Le, C. V. (2015). Cooperative joint inversion of 3D seismic and magnetotelluric data: With application in a mineral province. *Geophysics*, *80*(4), R175–R187.

Tarantola, A. (2005). *Inverse problem theory and methods for model parameter estimation* (Vol. 89). siam.

Ten Grotenhuis, S. M., Drury, M. R., Spiers, C. J., & Peach, C. J. (2005). Melt distribution in olivine rocks based on electrical conductivity measurements. *Journal of Geophysical Research: Solid Earth*, *110*(B12). doi: 10.1029/2004JB003462

Tesauro, M., Kaban, M. K., & Aitken, A. R. (2020). Thermal and compositional anomalies of the Australian upper mantle from seismic and gravity data. *Geochemistry, Geophysics, Geosystems*, *21*(11), e2020GC009305.

Thiel, S., & Heinson, G. (2013). Electrical conductors in Archean mantle—result of plume interaction? *Geophysical Research Letters*, *40*(12), 2947–2952.

Trampert, J., Vacher, P., & Vlaar, N. (2001). Sensitivities of seismic velocities to temperature, pressure and composition in the lower mantle. *Physics of the Earth and Planetary Interiors*, *124*(3-4), 255–267.

Van Wijk, J., Baldridge, W., Van Hunen, J., Goes, S., Aster, R., Coblentz, D., ... Ni, J. (2010). Small-scale convection at the edge of the Colorado Plateau: Implications for topography, magmatism, and evolution of Proterozoic lithosphere. *Geology*, *38*(7), 611–614.

Wannamaker, P. E., Evans, R. L., Bedrosian, P. A., Unsworth, M. J., Maris, V., & McGary, R. S. (2014). Segmentation of plate coupling, fate of subduction fluids, and modes of arc magmatism in Cascadia, inferred from magnetotelluric resistivity. *Geochemistry, Geophysics, Geosystems*, *15*(11), 4230–4253.

Wannamaker, P. E., Hasterok, D. P., Johnston, J. M., Stodt, J. A., Hall, D. B., Sodergren, T. L., ... others (2008). Lithospheric dismemberment and magmatic processes of the Great Basin–Colorado Plateau transition,Utah, implied from magnetotellurics. *Geochemistry, Geophysics, Geosystems*, *9*(5).

Wellman, P., & McDougall, I. (1974). Cainozoic igneous activity in eastern Australia. *Tectonophysics*, *23*(1-2), 49–65.

Williams, C. K., & Rasmussen, C. E. (1996). Gaussian processes for regression. In *Advances in neural information processing systems* (pp. 514–520).

Withers, A. C., Bureau, H., Raepsaet, C., & Hirschmann, M. M. (2012). Calibration of infrared spectroscopy by elastic recoil detection analysis of h in synthetic olivine. *Chemical Geology*, *334*, 92–98.

Xu, B., Griffin, W. L., Xiong, Q., Hou, Z.-Q., O'Reilly, S. Y., Guo, Z., ... Zheng, Y.-C. (2017). Ultrapotassic rocks and xenoliths from South Tibet: Contrasting styles of interaction between lithospheric mantle and asthenosphere during continental collision. *Geology*, *45*(1), 51–54.

Yaxley, G., Crawford, A., & Green, D. (1991, 11). Evidence for carbonatite metasomatism in spinel peridotite xenoliths from western Victoria, Australia. *Earth and Planetary Science Letters*, *107*, 305-317. Retrieved from https://linkinghub.elsevier.com/retrieve/pii/0012821X9190078V doi: 10.1016/0012-821X(91)90078-V

Yaxley, G., Green, D., & Kamenetsky, V. (1998, 11). Carbonatite metasomatism in the Southeastern Australian lithosphere. *Journal of Petrology*, *39*, 1917-1930. Retrieved from http://dx.doi.org/10.1093/petroj/39.11-12.1917 (10.1093/petroj/39.11-12.1917)

Yoshino, T. (2010). Laboratory electrical conductivity measurement of mantle minerals. *Surveys in Geophysics*, *31*(2), 163–206.

Young, M., Cayley, R., McLean, M., Rawlinson, N., Arroucau, P., & Salmon, M. (2013). Crustal structure of the east gondwana margin in southeast australia revealed by transdimensional ambient seismic noise tomography. *Geophysical Research Letters*, *40*(16), 4266–4271.

Yu, Y., Xu, X.-S., Griffin, W. L., O'Reilly, S. Y., & Xia, Q.-K. (2011). H2O contents and their modification in the Cenozoic subcontinental lithospheric mantle beneath the Cathaysia block, SE China. *Lithos*, *126*(3-4), 182–197.

Zhang, M., & O'Reilly, S. Y. (1997). Multiple sources for basaltic rocks from Dubbo, eastern Australia: geochemical evidence for plume—lithospheric mantle interaction. *Chemical Geology*, *136*(1-2), 33–54.

Zhang, M., Stephenson, P., O'REILLY, S. Y., McCULLOCH, M. T., & Norman, M. (2001). Petrogenesis and geodynamic implications of late Cenozoic basalts in North Queensland, Australia: trace-element and Sr–Nd–Pb isotope evidence. *Journal of Petrology*, *42*(4), 685–719.

Zlotnik, S., Afonso, J. C., Díez, P., & Fernández, M. (2008). Small-scale gravitational instabilities under the oceans: Implications for the evolution of oceanic lithosphere and its expression in geophysical observables. *Philosophical magazine*, *88*(28-29), 3197–3217.